Electrical conductivity of continental lithospheric mantle from integrated geophysical and petrological modeling: Application to the Kaapvaal Craton and Rehoboth Terrane, southern Africa

J. Fullea,[1] M. R. Muller,[1] and A. G. Jones[1]

Received 24 May 2011; revised 26 June 2011; accepted 7 July 2011; published 11 October 2011.

[1] The electrical conductivity of mantle minerals is highly sensitive to parameters that characterize the structure and state of the lithosphere and sublithospheric mantle, and mapping its lateral and vertical variations gives insights into formation and deformation processes. We review state-of-the-art conductivity models based on laboratory studies for the most relevant upper mantle minerals and define a bulk conductivity model for the upper mantle that accounts for temperature, pressure, and compositional variations. The bulk electrical conductivity model has been integrated into the software package LitMod, which allows for petrological and geophysical modeling of the lithosphere and sublithospheric upper mantle within an internally consistent thermodynamic-geophysical framework. We apply our methodology to model the upper mantle thermal structure and hydrous state of the western block of the Archean Kaapvaal Craton and the Proterozoic Rehoboth Terrane, in southern Africa, integrating different geophysical and petrological observables: namely, elevation, surface heat flow, and magnetotelluric and xenolith data. We find that to fit the measured magnetotelluric responses in both the Kaapvaal and Rehoboth terranes, the uppermost depleted part of the lithosphere has to be wetter than the lowermost melt-metasomatized and refertilized lithospheric mantle. We estimate present-day thermal lithosphere-asthenosphere boundary (LAB) depths of 230–260 and 150 ± 10 km for the western block of the Kaapvaal and Rehoboth terranes, respectively. For the Kaapvaal, the depth of the present-day thermal LAB differs significantly from the chemical LAB, as defined by the base of a depleted mantle, which might represent an upper level of melt percolation and accumulation within the lower lithosphere.

Citation: Fullea, J., M. R. Muller, and A. G. Jones (2011), Electrical conductivity of continental lithospheric mantle from integrated geophysical and petrological modeling: Application to the Kaapvaal Craton and Rehoboth Terrane, southern Africa, *J. Geophys. Res.*, *116*, B10202, doi:10.1029/2011JB008544.

1. Introduction

[2] The electrical conductivity of a material, σ (S/m), or its inverse, electrical resistivity, ρ (Ωm), is a measure of the medium's ability to conduct an electric current. The electrical conductivity of mantle minerals is sensitive to temperature and compositional variation [e.g., *Jones et al.*, 2009a] and, hence, has been used in attempts to characterize lithospheric and mantle structures. The major upper mantle mineral phases (e.g., olivine, pyroxenes, and garnet) exhibit insulator-like electrical behavior at low temperatures. However, at the temperatures prevalent in the upper mantle (i.e., 500°C < T < 1520°C), the electrical conductivity of the mantle minerals can be adequately described as an activated process, or processes, in a semiconductor and, therefore, characterized by an Arrhenius-type power law:

$$\sigma = \sigma_0 \exp\left(\frac{-\Delta H}{k_B T}\right), \quad (1)$$

where σ_0 (S/m) is a preexponential term, ΔH (eV) the activation enthalpy, T (K) is the temperature, and k_B (eV/K) is Boltzmann's constant. The activation enthalpy comprises the activation energy, ΔU (eV), and an additional term that accounts for the pressure dependence:

$$\Delta H = \Delta U + P\Delta V, \quad (2)$$

where ΔV (cm^3/mol) is the activation volume and P (GPa) is the pressure. The conduction mechanism in this temperature range changes at around 1300°C–1500°C from small polaron (electron hopping between ferric Fe^{3+} and ferrous Fe^{2+} ions) at T < 1300°C, to ionic conduction (charge car-

[1]Dublin Institute for Advanced Studies, Dublin, Ireland.

0148-0227/11/2011JB008544

riers are magnesium vacancies) [e.g., *Schock et al.*, 1989; *Yoshino et al.*, 2008a]. In the case of the small polaron mechanism the activation enthalpies are around 1.6 eV, whereas for ionic conduction, values of >2 eV are typically expected [e.g., *Yoshino et al.*, 2008a, 2009; *Farla et al.*, 2010].

[3] As expressed by equation (1), electrical conductivity is governed, to first order, by temperature variation. However, there are other variables (i.e., composition, partial melt and/or water content in the solid phase and the melt) that affect electrical conductivity to lesser or greater extent. It is well known that chemical substitution of magnesium by iron in the dodecahedral site of silicate minerals, without changes in the lattice symmetry, increases electrical conductivity [e.g., *Hinze et al.*, 1981; *Seifert et al.*, 1982; *Omura et al.*, 1989; *Romano et al.*, 2006]. The amount of iron, either for the whole rock or for the individual mineral constituents, is usually described by the magnesium number, Mg # = Mg/(Mg + Fe), or its converse, the iron content, $X_{Fe} = 1 - Mg\ \#/100$, where Mg and Fe refer to the molar concentrations of those elements. Another factor that can potentially enhance electrical conductivity is the presence of an interconnected melt fluid in the lithospheric or sublithospheric mantle, either a silicate melt [e.g., *Tyburczy and Waff*, 1983; *Toffelmier and Tyburczy*, 2007; *Pommier et al.*, 2008] or a carbonatite melt [*Gaillard et al.*, 2008]. The connectivity of carbonatite melt is larger than that of silicate melt [e.g., *Hammouda and Laporte*, 2000]. Laboratory studies suggest that the connectivity of basaltic melt can be significantly enhanced by anastomosing networks produced by stress-driven melt segregation [*Holtzman et al.*, 2003]. The existence of such a molten phase in the upper mantle depends on the solidus, which, in turns, can be significantly modified by the presence of volatiles (e.g., water, CO_2). Since *Karato* [1990] first proposed that the presence of even small amounts of water (protons bound to structural oxygen atoms at the ppm level) in the nominally anhydrous minerals (e.g., olivine and its high-pressure polymorphs, pyroxenes and garnet) could significantly increase mineral conductivity, several laboratory studies have been carried out to investigate and quantify the electrical behavior of hydrogen-bearing nominally anhydrous minerals [e.g., *Wang et al.*, 2006; *Yoshino et al.*, 2009]. The results of these experiments are controversial [see *Karato and Dai*, 2009; *Yoshino*, 2010] yet convergent in their conclusion that at high pressure, dissolved water considerably enhances electrical conductivity of nominally anhydrous minerals.

[4] The presence of dissolved water is also a potential source of significant and observable electrical anisotropy. Dry olivine single crystals are only weakly anisotropic [e.g., *Du Frane et al.*, 2005], but the presence of water can increase anisotropy by as much as 1 order of magnitude for 1000 wt ppm according to laboratory results [*Poe et al.*, 2010]. If proton conduction in olivine single crystals is adequately described by the Nernst-Einstein equation, then the conductivity should be proportional to the diffusivity of protons in olivine. The diffusion of protons in the olivine lattice is a process dominated by the interaction of protons with polarons at temperatures <900°C, and by the proton-metal vacancy interaction at temperatures >900°C [e.g., *Kohlstedt and Mackwell*, 1998; *Demouchy and Mackwell*, 2006]. Both the low- and high-temperature diffusion regimes are strongly anisotropic, but in both regimes the fast diffusion axis seems to be at odds with the high electrical conductivity axis in olivine observed in the most recent and detailed laboratory measurements at pressure above 6 GPa [*Poe et al.*, 2010]. Moreover, macroscopic anisotropy in olivine (or other mineral phase) aggregates requires significant alignment of the single crystals, i.e., crystal or shape preferred orientation produced by dislocation creep mantle deformation [e.g., *Gatzemeier and Tommasi*, 2006].

[5] The bulk or whole rock conductivity is a function of the individual contribution of its mineral constituents. There are several mixing theories that can be used to determine the conductivity of the mineral assemblage in the lithospheric mantle according to the mineral abundances and their geometrical distribution [e.g., *Xu et al.*, 2000; *Ledo and Jones*, 2005; *Jones et al.*, 2009a]. As the textural information in natural mantle rocks is only scarcely and inadequately sampled (xenoliths and peridotite massifs) and remains poorly known, in this work we adopt solutions that invoke no assumptions regarding the phase geometry: the series and parallel solutions [e.g., *Xu et al.*, 2000] and the Hashin-Shtrikman bounds [e.g., *Ledo and Jones*, 2005; *Jones et al.*, 2009a].

[6] The magnetotelluric (MT) method is a natural source electromagnetic method used to image the Earth from the near surface (100 m) to deep within the mantle (>1000 km). It is based on the relation between the temporal variations of the Earth's electric and magnetic fields, and its subsurface electrical resistivity structure [e.g., *Jones*, 1999]. The objective of MT modeling is to obtain the conductivity-resistivity distribution laterally and with depth by the inversion of the complex frequency-dependent impedance tensor responses that are usually displayed as apparent resistivities and phases. A common caveat associated with most MT inversions is that while they predict perfectly valid models, these models are not necessarily directly related to real, or what we can estimate as real, petrophysical conditions inside the Earth because of resolution issues. For example, although for a one-dimensional (1-D) Earth there exists a uniqueness theorem for perfect data at all frequencies [*Bailey*, 1970], data insufficiency and inaccuracy lead to highly nonlinear resolution of model parameters. Particularly, the true resistivity of a resistive layer or region beneath a more conducting one is very difficult to resolve because of the screening effect of the upper layer. Thus, only a lower bound on the resistivity of the mantle directly below the crust can usually be set [*Jones*, 1999]. Therefore, the link between the inferred conductivity models and other fundamental variables, such as temperature, pressure or composition (i.e., iron and water content), which, according to laboratory studies, fully characterize the electrical conductivity, is often missed.

[7] In this work we propose a more petrophysically driven approach to modeling MT data based on the approach governing the software package LitMod [*Fullea et al.*, 2009]. This software combines petrological and geophysical modeling of the lithosphere and sublithospheric upper mantle within an internally consistent thermodynamic-geophysical framework, where all relevant mantle properties (e.g., density and seismic velocities) are functions of temperature, pressure and composition. In the first part of the paper we review state-of-the-art electrical conductivity

models based on laboratory studies for the predominant upper mantle minerals and define a bulk resistivity model dependent on temperature, pressure and composition (i.e., mineral percentages, iron and water content). In the second part we study the upper mantle structure of two Precambrian regions in southern Africa: the Archean Kaapvaal Craton and the Proterozoic Rehoboth Terrane. We generate self-consistent lithospheric/sublithospheric mantle models of the two domains that simultaneously fit a suite of geophysical and petrological observables: namely, elevation, surface heat flow (SHF), MT, and xenolith data.

2. The Electrical Conductivity of Mantle Minerals

[8] In this study we use the software package LitMod to define realistic temperature and pressure distributions within the upper mantle, and to characterize the mineral assemblages given the bulk chemical compositions. Geotherms are computed under the assumption of steady state in the lithospheric mantle, considering a P-T-dependent thermal conductivity [see *Fullea et al.*, 2009, Appendix A1]. In the sublithospheric mantle an adiabatic thermal gradient is assumed, and between the lithosphere and sublithospheric mantle we assume a 50 km thick "transition" region with a continuous linear superadiabatic gradient (i.e., heat transfer is controlled by both conduction and convection [see *Fullea et al.*, 2009, Appendix A2]. The pressure-density coupling is solved with a full iterative scheme [see *Fullea et al.*, 2009, section 2.3]. In the mantle, stable mineral assemblages are computed according to a Gibbs free energy minimization strategy for one or more zones or layers, each of which is defined in terms of its major element composition in the system Na_2O-TiO_2-FeO-CaO-MgO-Al_2O_3-SiO_2 [*Connolly*, 2005; *Afonso et al.*, 2008]. In this way, bulk rock properties, such as density and seismic velocity, are determined consistently within the mantle using an appropriate averaging of the mineral phase constituent's contribution. All the stable assemblages in this study are computed using a modified-augmented version of *Holland and Powell*'s [1998] thermodynamic database. In particular, a solid solution model for the solubility of pyroxenes into garnet and the high-pressure monoclinic polymorph of orthopyroxene with C2/c symmetry were added [see *Afonso and Zlotnik*, 2011, Appendix A6].

[9] Careful and controlled laboratory studies at the temperatures and pressures relevant to the upper mantle are essential to understand the electrical behavior of the mantle mineral constituents in situ. Such measurements have been taking place since the 1960s; see the review of early work by *Duba* [1976] and other reviews over the last 30 years by *Hinze* [1982], *Laštovičková* [1983, 1991], *Nover* [2005], and *Yoshino* [2010]. In recent years, considerable effort has been expended in designing suitable experiments to measure the electrical properties of many of the mantle minerals under various conditions [e.g., *Wang et al.*, 2006; *Dai and Karato*, 2009a; *Yoshino et al.*, 2009]. In this section we review the state-of-the-art conductivity models for olivine, pyroxenes and garnet, as the most representative minerals in the mantle down to the 410 km discontinuity [e.g., *Ringwood*, 1975; *Irifune and Ringwood*, 1987]. Both electrical conductivity and its inverse, electrical resistivity, are referred to in the literature, with an emphasis on the former in laboratory measurements. Conversely, most electromagnetic (EM) surveys, particularly MT, report resistivity to avoid the small fraction conductivity values. Both representations are equivalent and we will employ them interchangeably throughout this paper.

[10] In order to compare meaningfully different laboratory-derived conductivity formulations at relevant conditions (i.e., temperature, pressure and composition) we assume a continental lithosphere characterized by crustal and lithospheric thicknesses of 43 and 180 km, respectively (called the reference lithospheric column hereafter) (Figure 1). We impose a realistic chemical layering in the lithospheric mantle to illustrate the influence of compositional variations in conductivity: an upper mantle layer, i.e., $z < 120$ km and Mg # = 92.2, is relatively depleted with respect to a lower more fertile one, i.e., $120 < z < 180$ km and Mg # = 90.5, and to the sublithospheric mantle, i.e., $z > 180$ km and Mg # = 89.3 (see Table 1). The associated temperature, mineral assemblage, and iron content distributions with depth are shown in Figure 1.

2.1. Olivine

[11] Olivine is by far the most abundant mineral constituent of the upper mantle down to the 410 km discontinuity (Figure 1d) and, therefore, its conductivity has been extensively studied as representative of the bulk lithospheric mantle conductivity [see *Jones et al.*, 2009a, and references therein].

[12] One of the most robust attempts to provide an accurate description of the olivine electrical conductivity as a function of iron content is the work by *Hirsch et al.* [1993]. Electrical conductivity of a synthetic dry single olivine crystal was measured in the temperature range 1150°C–1300°C ([100] axis) under controlled thermodynamic conditions and for a variety of iron contents ($X_{Fe} = 0.09$–0.34). The following relation was derived for olivine conductivity:

$$\sigma = \frac{\sigma_0 X_{Fe}^{1.81}}{T} \exp\left(\frac{-E_a}{k_B T}\right), \tag{3}$$

where $\sigma_0 = 10^{6.54}$ (S K/m) and $E_a = 1.35$ eV [*Hirsch et al.*, 1993]. Iron content dependence is only present in the pre-exponential factor and is absent in the activation energy (equation (3)). The rationale for the latter, according to the authors, is that the activation energy is dominated by the effective activation energy for charge carriers (polarons) that were not reported to be X_{Fe} dependent at the experimental conditions studied [*Hirsch et al.*, 1993].

[13] Another widely used reference is the SO2 model for olivine conductivity [*Constable et al.*, 1992]. In this model the geometric average of the conductivity along the three crystallographic directions in a dry single olivine crystal is given by the sum of two thermally activated processes with their corresponding activation energies:

$$\sigma_{SO2} = \sigma_{01} \exp\left(\frac{-E_{a1}}{k_B T}\right) + \sigma_{02} \exp\left(\frac{-E_{a2}}{k_B T}\right), \tag{4}$$

where $\sigma_{01} = 10^{2.402}$ S/m, $E_{a1} = 1.6$ eV, $\sigma_{02} = 10^{9.17}$ S/m, and $E_{a2} = 4.25$ eV. An improved version of this model, partic-

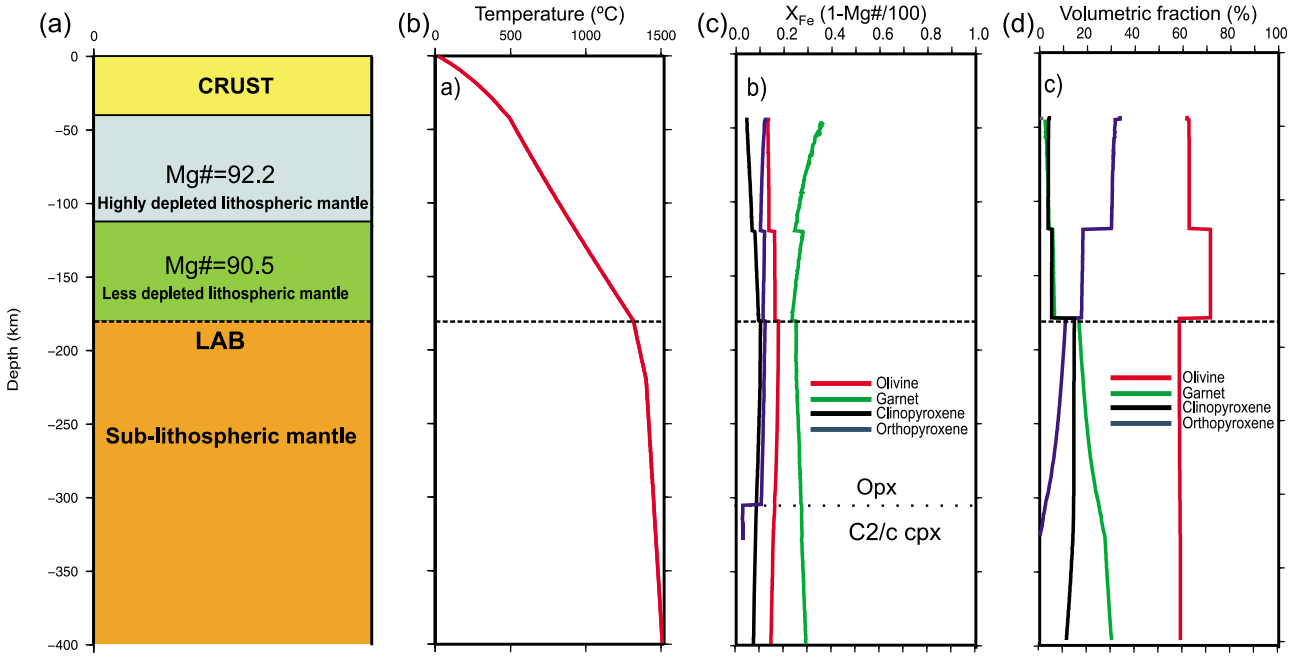

Figure 1. (a) Reference lithospheric structure assumed to compare the electrical conductivity of mantle minerals according to different experimental results (see the text for further details). The associated (b) temperature, (c) iron content, and (d) mineral assemblage distributions are determined using the software LitMod [*Fullea et al.*, 2009].

ularly in the temperature range of 1300°C–1500°C (i.e., in the sublithospheric mantle) is the SEO3 reference model [*Constable*, 2006]. This latter publication integrated thermopower and conductivity data from a dunite rock that included small amounts of pyroxene. The main advantage of SEO3 with respect to SO2 is the natural averaging over the three olivine axes, and the natural buffer for silicon. The model also includes an improved description of the high-temperature conduction mechanisms for magnesium vacancies [*Constable*, 2006]. Reordering the different terms in SEO3, the dry olivine conductivity is described by:

$$\sigma_{SEO3} = \sigma_{01}\exp\left(\frac{-E_{a1}}{k_B T}\right) + \sigma_{02}\exp\left(\frac{-E_{a2}}{k_B T}\right) + \left[A_1\exp\left(\frac{-E_{a3}}{k_B T}\right) + A_2\exp\left(\frac{-E_{a4}}{k_B T}\right)\right] fO_2^{1/6}, \quad (5)$$

where $\sigma_{01} = 10^{0.995}$ S/m, $E_{a1} = 1.407$ eV, $\sigma_{02} = 10^{2.601}$ S/m, $E_{a2} = 1.842$ eV, $A_1 = 10^{0.814}$ S/(m Pa$^{1/6}$), $E_{a3} = 1.07$ eV, $A_2 = 10^{6.733}$ S/(m Pa$^{1/6}$) and $E_{a4} = 2.92$ eV. Another difference with respect to the previous SO2 model is the inclusion of oxygen fugacity dependence (third term in equation (5)). The oxygen fugacity, fO_2 (Pa), constrains the redox state in the mantle and, therefore, the density of polarons. In general it is assumed that under upper mantle conditions the oxygen fugacity, which depends mainly on temperature, is close to the QFM (quartz-fayalite-magnetite) buffer. A different fugacity dependence, fO_2 to the power 2/11, was reported by *Du Frane et al.* [2005] on the basis of electrical conductivity measurements of a single crystal of San Carlos olivine ($X_{Fe} = 0.1$) over oxygen fugacities in the range 10^{-7} Pa < fO_2 < 10^{1} Pa and T = 1100°C–1300°C. The geometrical mean of the conductivity along the three crystallographic axes according to *Du Frane et al.* [2005] is

$$\sigma_{GM-DF} = \left(2.51 fO_2^{2/11} + 0.0653\right)\exp\left(\frac{-E}{k_B T}\right), \quad (6)$$

where fO_2 is in atm and E = 0.531 eV [*Du Frane et al.*, 2005]. The experimental study of *Du Frane et al.* [2005] was performed using iron-doped Pt electrodes to avoid iron loss from the sample to the electrodes which would result in a decrease of the polaron population. These authors claim that the effect of iron loss in previous observations

Table 1. Bulk Mantle Compositions Used in This Study

	Average Kaapvaal Harzburgite (wt %)	Average Kaapvaal Low-T Lherzolite (wt %)	Average Kaapvaal High-T Lherzolite (wt %)	PUM M-S95 (wt %)[a]
SiO_2	45.9	46.5	44.4	45.0
TiO_2	0.05	0.05	0.17	0.20
Al_2O_3	1.30	1.40	1.75	4.50
Cr_2O_3	0.34	0.34	0.30	0.38
FeO	6.00	6.60	8.10	8.10
MnO	0.10	0.10	0.12	0.14
MgO	45.5	43.8	43.4	37.8
CaO	0.50	0.86	1.27	3.60
Na_2O	0.07	0.10	0.12	0.36
NiO	0.28	0.29	0.26	0.25
Mg #	93.1	92.2	90.5	89.3
Cr/(Cr + Al)	0.27	0.14	0.10	0.05

[a]PUM stands for primitive upper mantle; M-S95 refers to *McDonough and Sun* [1995].

could underestimate the measured conductivity by up to 0.15 log units.

[14] The conductivity of mantle-derived San Carlos olivine was also measured in the temperature range 1000°C–1400°C for sublithospheric mantle pressures (4–10 GPa) by *Xu et al.* [2000], who added 5 wt % opx to the sample in order to buffer silica activity. The conductivity of the sample analyzed by *Xu et al.* [2000], which was dry and representative of a bulk Mg # around 90 (i.e., $X_{Fe} = 0.1$), fitted equation (1) with the following parameters: $\sigma_0 = 10^{2.69}$ S/m, $\Delta U = 1.62$ eV and $\Delta V = 0.68$ cm^3/mol. A more recent study by the same group on dry San Carlos polycrystalline olivine buffered by 2% opx determined very similar values (at T = 600°C–1000°C and P = 4 GPa) for the conductivity of dry samples [*Wang et al.*, 2006]. These authors also reported a significant increase in conductivity if hydrogen was dissolved in the lattice, proposing the following formulation:

$$\sigma = \sigma_0 \exp\left(\frac{-\Delta H}{k_B T}\right) + A C_w^r \exp\left(\frac{-\Delta H_{wet}}{k_B T}\right), \quad (7)$$

where $\sigma_0 = 10^{2.4}$ S/m, $\Delta H = 1.6$ eV, $A = 10^3$ S/m, $\Delta H_{wet} = 0.9$ eV, C_w (wt %) is the water content, and r = 0.62. Neither pressure nor water content dependence was reported for the activation enthalpies in equation (7) [*Wang et al.*, 2006].

[15] On the basis of the measurements of olivine conductivity for different iron contents by *Hinze et al.* [1981], *Vacher and Verhoeven* [2007] revisited the conductivity model of *Xu et al.* [2000], proposing a new parameterization of the iron content:

$$\sigma = \sigma_0 \left(\frac{X_{Fe}}{X_{Fe\,ref}}\right)^{\alpha} \exp\left(\frac{-\left(\Delta H_{ref} + \beta[X_{Fe} - X_{Fe\,ref}]\right)}{k_B T}\right), \quad (8)$$

where $\sigma_0 = 10^{2.69}$, $X_{Fe\ ref} = 0.1$, $\Delta H_{ref} = 1.62$ eV, and $\alpha = 2.42$ and $\beta = -0.48$ are two parameters that control the power law and linear iron content dependence of the pre-exponential term and the activation energy, respectively. Both parameters α and β are calculated by *Vacher and Verhoeven* [2007] using the data of *Xu et al.* [2000] at $X_{Fe} = 0.1$ as a benchmark or reference value.

[16] A recent laboratory study on San Carlos olivine aggregates (Mg # = 92.5) identified three different conduction mechanisms according to the temperature [*Yoshino et al.*, 2009]:

$$\sigma = \sigma_{0i} \exp\left(\frac{-\Delta H_i}{k_B T}\right) + \sigma_{0h} \exp\left(\frac{-\Delta H_h}{k_B T}\right) + \sigma_{0p} C_w \exp\left(\frac{-\left(\Delta H_0 - \alpha C_w^{1/3}\right)}{k_B T}\right), \quad (9)$$

where $\sigma_{0i} = 10^{4.73}$ S/m, $\Delta H_i = 2.31$ eV, $\sigma_{0h} = 10^{2.98}$ S/m, $\Delta H_h = 1.71$ eV, $\sigma_{0p} = 10^{1.9}$ S/m, $\Delta H_0 = 0.92$ eV, and $\alpha = 0.16$ [*Yoshino et al.*, 2009]. The first term in equation (9) represents ionic conduction (T > 1430°C), the second term is for small polaron conduction (730°C < T < 1430°C), and the third term is for proton conduction (T < 730°C). A water content–dependent activation enthalpy for the proton conduction term (equation (9)) was similarly suggested by *Poe et al.* [2010]. These authors studied the electrical conductivity of single-crystal San Carlos olivine (Mg # = 90) at 8 GPa and T < 700°C for a variety of water contents and concluded that for elevated concentrations of dissolved water (i.e., hundreds of weight parts per million H_2O, wt ppm) the conductivity along the [010] axis is about an order of magnitude higher than along the [001] axis. This represents a stronger water content dependence than that suggested by *Yoshino et al.* [2009], at least for elevated water contents, with the greatest effect being along the [010] *b* axis of olivine rather than the [100] *a* axis. More specifically, *Poe et al.* [2010] fit the third term of equation (9) with the following values for each crystallographic direction: $\sigma_{0p[100]} = 10^{2.57}$ S/m, $\sigma_{0p[010]} = 10^{3.46}$ S/m, $\sigma_{0p[001]} = 10^{1.02}$ S/m, $\Delta H_{0[100]} = 1.26$ eV, $\Delta H_{0[010]} = 1.5$ eV, $\Delta H_{0[001]} = 0.81$ eV and $\alpha_{[100]} = 1.18$, $\alpha_{[010]} = 1.43$, $\alpha_{[001]} = 0.7$.

[17] In order to make a meaningful comparison, we calculate isotropic conductivities according to the laboratory studies reviewed above assuming the geotherm, pressure, and olivine iron content distributions of our reference lithospheric column as shown in Figure 1. The olivine conductivities under dry conditions for the different models introduced in this section are plotted in Figure 2a. With the exception of the model of *Du Frane et al.* [2005], the maximum difference between the models is around 1.36 log units at the base of the crust (assumed to be the Moho), T = 495°C. The most resistive model down to 160 km depth (T = 1190°C) is SE03 [*Constable*, 2006] (equation (5)), whereas at greater depths it is the SO2 model [*Constable et al.*, 1992]. Above T = 1000°C the model of *Du Frane et al.* [2005] is far more conductive than the rest of the models (up to 2.1–3.5 log units at the Moho). *Du Frane et al.* [2005] attribute this behavior to the elevated value of the iron defect concentration. In the temperature range 1480°C > T > 1000°C, i.e., the lithosphere-asthenosphere transition zone, the most conductive model is that of *Vacher and Verhoeven* [2007].

[18] A common characteristic in all the conductivity models is that the leading variable is temperature. As a consequence, the strongest variations in electrical conductivity occur in the lithosphere (i.e., the thermally conductive domain) where temperature increases from 495°C at the base of the crust to 1315°C at the lithosphere-asthenosphere boundary (LAB) (Figure 1b). Logarithmic resistivities ($\log_{10}(\rho\ [\Omega m])$) within the lithosphere range from 6.76 to 8.20 at the Moho (4.66 for the *Du Frane et al.* [2005] model) to 1.78–2.67 at the LAB, a change of 5 orders of magnitude or more for a change of 820°C in temperature, making conductivity the most sensitive physical parameter to temperature variation. From the LAB downward (i.e., in the sublithospheric mantle) the thermal regime transitions to an adiabatic gradient, and temperature increase with depth is at a far lower gradient than in the lithosphere. Therefore, the $\log_{10}(\rho)$ values decrease more slowly in the sublithospheric mantle than in the lithosphere for all the models (Figure 2a). The maximum decrease of olivine resistivity in the sublithospheric mantle corresponds to models that include an ionic conduction term (i.e., Mg vacancies) for high temperatures: SE03 [*Constable*, 2006] and the model of *Yoshino et al.* [2009], amounting to a 0.99 and 0.68 decrease in $\log_{10}(\rho)$, respectively, between the LAB and the 410 km discontinuity. Models assuming conduction only due to small polarons [e.g., *Wang et al.*, 2006] or based on single-crystal olivine measurements lacking a pyroxene buffer (SO2 [*Constable et al.*, 1992] and the model of *Du Frane*

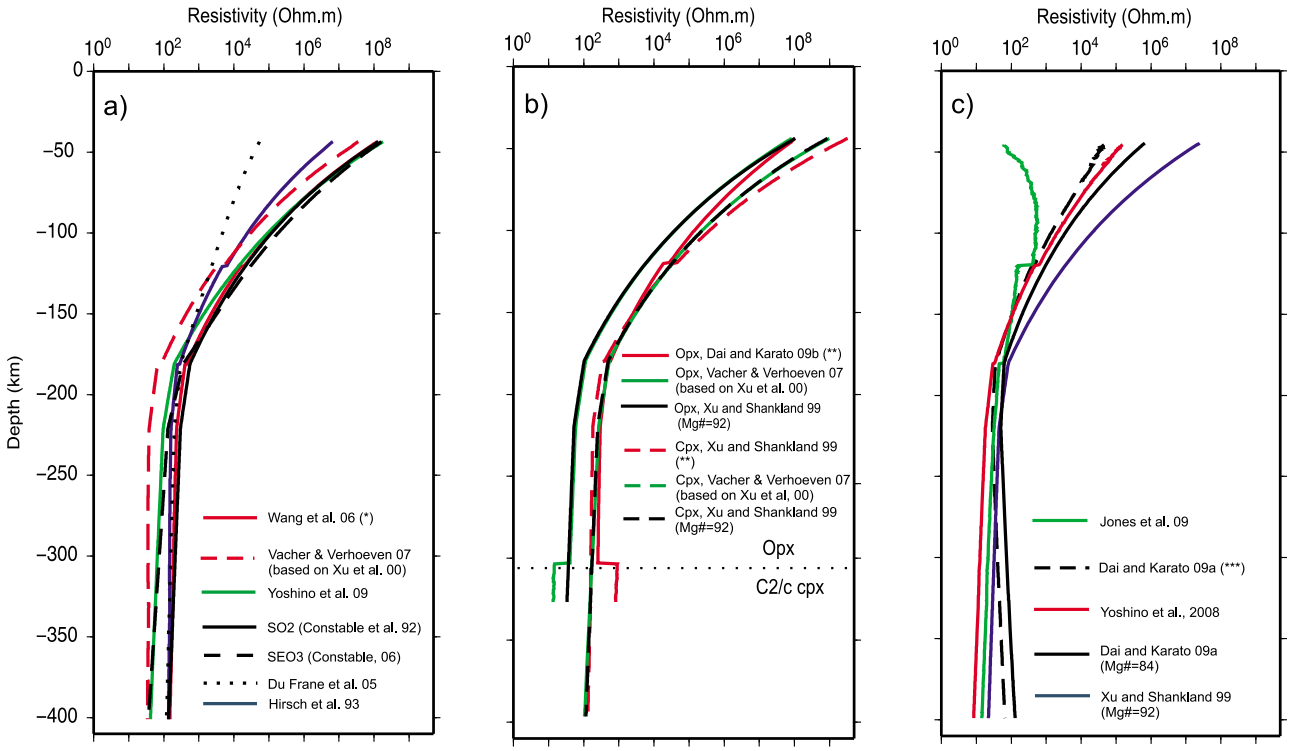

Figure 2. Comparison of different laboratory results for the electrical resistivity of (a) olivine, (b) pyroxenes, and (c) garnet under dry conditions (see the text for further details). Temperature, pressure, and iron content are taken from the reference lithospheric column of Figure 1. The single asterisk (*) indicates a modified version of the olivine resistivity model of *Wang et al.* [2006] to include an iron content-dependent activation enthalpy based on the measurements made by *Omura et al.* [1989] (see Figure 3). The double asterisks (**) indicate modified versions of *Dai and Karato*'s [2009b] and *Xu and Shankland*'s [1999] models for orthopyroxene and clinopyroxene, respectively, integrating the activation enthalpy as a function of iron content (after *Seifert et al.* [1982]; see Figure 3). The triple asterisk (***) indicates a modified version of *Dai and Karato*'s [2009b] garnet resistivity model including measurements for the activation enthalpy as a function of iron content (after *Romano et al.* [2006]; see Figure 3).

et al. [2005]) show a decrease of resistivity of lesser extent, namely, 0.40–0.61 log units. A further implication of the reduced thermal gradient in the sublithospheric mantle is that the effect of pressure, via the activation volume, is not negligible. In particular, the model of *Wang et al.* [2006] predicts a decrease in $\log_{10}(\rho)$ of 0.35 if an activation volume of 0.68 cm^3/mol is assumed [*Xu et al.*, 2000] and of 0.52 if the pressure effect is ignored. Therefore, in the sublithospheric mantle the effect of pressure in olivine conductivity via the activation volume [*Xu et al.*, 2000] is of the same order of magnitude but is opposite in sense, compared with the ionic conduction term [e.g., *Yoshino et al.*, 2009]. Regarding the absolute values, the models based on single-crystal measurements (*Hirsch et al.* [1993], SO2 [*Constable et al.*, 1992], and *Du Frane et al.* [2005] models) tend to predict a more resistive sublithospheric mantle (T > 1315°C) than those including a pyroxene buffer (SE03 [*Constable*, 2006], *Yoshino et al.* [2009], and *Vacher and Verhoeven* [2007] models). For instance, at the bottom of the model (i.e., 400 km depth and T = 1510°C) the first group of models shows a resistivity of ~100 Ωm, compared with around 25 Ωm for the second group (Figure 2a).

[19] The iron partitioning in the different minerals for our reference lithospheric column is shown in Figure 1c. For olivine, X_{Fe} ranges between 0.13 and 0.18 with discontinuities (ΔX_{Fe} = 0.023–0.01) at the boundaries between the mantle layers with different compositions (see Table 1). The maximum X_{Fe} for olivine is present in the uppermost sublithospheric mantle, in the vicinity of the LAB. From the LAB to the bottom of the model (400 km) X_{Fe} decreases by almost one quarter. Olivine resistivity dependence on iron content (i.e., composition) is a second-order factor in comparison with temperature: the changes in $\log_{10}(\rho)$ in the lithosphere due to ΔX_{Fe} are 0.1–0.2 for those models that include X_{Fe} dependence [*Hirsch et al.*, 1993; *Vacher and Verhoeven*, 2007]. As an additional check on the conductivity dependence on X_{Fe} we fit the activation enthalpy obtained by *Omura et al.* [1989] for olivine with different iron contents to a third-order polynomial on X_{Fe}: $\Delta H(X_{Fe}) = a + b\,X_{Fe} + c\,X_{Fe}^2 + d\,X_{Fe}^3$ (Figure 3 and Table 2). A modified version of *Wang et al.*'s [2006] model, in which the X_{Fe}-dependent activation enthalpy derived from *Omura et al.*'s [1989] data has been incorporated, shows small differences in the lithosphere with respect to the alternative parameterizations of iron content (Figure 2a). The $\log_{10}(\rho)$ variation with X_{Fe} in

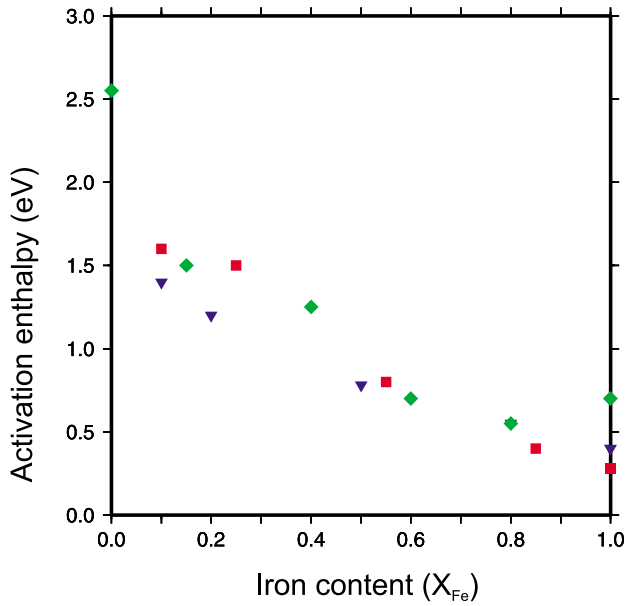

Figure 3. Activation enthalpy variation with mineral iron content. Symbols are as follows: squares show olivine [*Omura et al.*, 1989], triangles show pyroxenes [*Seifert et al.*, 1982], and diamonds show garnet [*Romano et al.*, 2006].

the lithosphere in the modified *Wang et al.* [2006] model is almost equal to that predicted by *Hirsch et al.* [1993] and is 0.12 log units lower than that of *Vacher and Verhoeven* [2007].

2.2. Pyroxenes

[20] The orthopyroxene phase (opx) in mantle peridotites is volumetrically important in the lithospheric mantle, particularly for relatively depleted compositions (typically 20%–35% volume fraction; see Figure 1d), whereas clinopyroxene (cpx) is rare to absent (0%–5% volume fraction) in the lithospheric mantle and relatively more abundant in the sublithospheric mantle (10%–15% volume fraction). Opx starts to dissolve into garnet in the sublithospheric mantle. At pressures around 10 GPa, opx is transformed into its high-pressure polymorph clinopyroxene with C2/c symmetry (C2/c cpx), which is almost totally dissolved into garnet at depths >330 km.

[21] The electrical conductivity of dry opx and cpx (Mg # = 92) were determined under controlled thermodynamic conditions using impedance spectroscopy in the temperature range of 1000°C–1400°C by *Xu and Shankland* [1999]. These authors fitted equation (1) with the following parameters: $\sigma_0 = 10^{3.72}$ S/m, $\Delta H = 1.8$ eV for opx and $\sigma_0 = 10^{3.25}$ S/m, $\Delta H = 1.87$ eV for cpx. A more recent laboratory study on opx single-crystal conductivity ($X_{Fe} = 0.14$–0.18) in the temperature range 600°C–1200°C also included the effect of water content [*Dai and Karato*, 2009b]. According to this more recent study, opx conductivity is weakly anisotropic and can be fit by equation (6) with the following parameters: $\sigma_0 = 10^{2.4}$ S/m, $\Delta H = 1.52$ eV, $A = 10^{2.6}$ S/m, $\Delta H_{wet} = 0.85$ eV, and $r = 0.62$. The iron content dependence of the conductivity of pyroxenes was studied by *Seifert et al.* [1982] under defined thermodynamic conditions at P = 1–2 GPa, and T = 500°C–1000°C. These data were used by *Vacher and Verhoeven* [2007], who assumed the opx conductivity model by *Xu and Shankland* [1999] at $X_{Fe} = 0.1$ as a reference, to fit equation (8) with the following parameters: $\sigma_0 = 10^{3.66}$ S/m, $X_{Fe\ ref} = 0.1$, $\Delta H_{ref} = 1.79$ eV, $\alpha = -1.28$, and $\beta = -1.41$ for opx and $\sigma_0 = 10^{3.19}$ S/m, $X_{Fe\ ref} = 0.1$, $\Delta H_{ref} = 1.86$ eV, $\alpha = -1.28$, and $\beta = -1.41$ for cpx. The electrical conductivity of pyroxenite (55% opx, 43% cpx, and 2% spinel + olivine, $X_{Fe} = 0.06$–0.1) was measured at T = 800°C–1200°C and P = 1–4 GPa using different solid buffers to control oxygen fugacity by *Dai et al.* [2006]. According to these authors, the conductivity of pyroxenite for the Mo + MoO_2 buffer can be fit by equation (1) with the following parameters: $\sigma_0 = 10^{3.25}$ S/m and $\Delta H = 1.79$ eV, which are very similar to the values reported by *Xu and Shankland* [1999] for the preexponential term and activation enthalpy of cpx and opx, respectively. No significant pressure dependence on the activation enthalpy was reported by *Dai et al.* [2006].

[22] The different conductivity models for opx and cpx, determined according to the geotherm and the iron partitioning associated with our reference lithospheric column (Figure 1), are given in Figure 2b. In the absence of experimental data we use the extant opx conductivity models as a proxy for the C2/c cpx conductivity. The X_{Fe} distribution with depth for opx remains almost constant at 0.1 with discontinuities ($\Delta X_{Fe} = 0.02$–0.01) at the boundaries between the mantle layers with different composition (see Table 1). For cpx, X_{Fe} ranges from 0.05 to 0.1, increasing from the Moho down to around P = 6.4 GPa (z = 200 km), and then decreasing downward. The X_{Fe} discontinuities for cpx are similar to those in opx. At P = 10 GPa (z = 300 km) opx is transformed into C2/c cpx which is relatively iron poor with $X_{Fe} = 0.025$ (Figure 2b).

[23] The electrical resistivity model of *Vacher and Verhoeven* [2007] is nearly coincident with the *Xu and Shankland* [1999] model for both opx (<0.06 log units difference) and cpx (<0.11 log units difference). The values of

Table 2. Small Polaron and Ionic Conduction Terms for the Bulk Conductivity Model of the Mantle Adopted in This Paper[a]

	log σ_0/log σ_{0i} (S/m)	a	b	c	d	e	f	ΔV (cm^3/mol)	ΔH_i (eV)
Ol[b]	2.4–3/4.73	1.642	0.246	−4.85	3.259	-	-	0.68	2.31
Opx[c]	2.4–3.72/–	1.9	−2.77	2.61	−1.09	-	-	-	-
Cpx[d]	3.25/–	2.075	−2.77	2.61	−1.09	-	-	-	-
Gnt[e]	(2.67–3.39) + log(1 − 0.044P(GPa))/4.96	2.6	−15.33	80.4	−194.6	202.6	−75	2.5	2.05

[a]See equation (11) and the text for further details.
[b]Olivine model based on the following sources: *Wang et al.* [2006], *Omura et al.* [1989], *Xu et al.* [2000], and *Yoshino et al.* [2009].
[c]Orthopyroxene model based on the following sources: *Dai and Karato* [2009b], *Seifert et al.* [1982], and *Xu and Shankland* [1999].
[d]Clinopyroxene model based on the following sources: *Xu and Shankland* [1999] and *Seifert et al.* [1982].
[e]Garnet model based on the following sources: *Dai and Karato* [2009a], *Romano et al.* [2006], and *Yoshino et al.* [2008b].

$\log_{10}(\rho)$, from the Moho down to the LAB, range from 8 to 2.7 log units and from 9 to 2.7 log units for opx and cpx, respectively. Excepting the model of *Dai and Karato* [2009b] below 150 km, opx is more conductive than cpx for its entire stability field. The modest iron content sensitivity in the conductivity model of *Vacher and Verhoeven* [2007] is due to the fact that the decrease of the activation energy for increasing X_{Fe} is balanced, and even exceeded, by the decrease of the preexponential term (i.e., negative α in equation (8)). This leads to situations in which the conductivity increases for decreasing X_{Fe} (compare the *Vacher and Verhoeven* [2007] and *Xu and Shankland* [1999] models for cpx at z > 300 km in Figure 2b). This behavior is at odds with the conductivity dependence on iron content of other minerals [e.g., *Omura et al.*, 1989; *Hinze et al.*, 1981; *Romano et al.*, 2006] and certainly with the X_{Fe} dependence exhibited by diopside itself [*Wang et al.*, 1999]. As an alternative approach, we integrate the iron content parameter in the conductivity of pyroxenes by fitting the activation enthalpies determined by *Seifert et al.* [1982] to a third-order polynomial having X_{Fe} as the variable: $\Delta H(X_{Fe}) = a + b\,X_{Fe} + c\,X_{Fe}^2 + d\,X_{Fe}^3$ (Figure 3 and Table 2). As the resulting activation enthalpies are slightly lower in comparison with previous work [*Xu and Shankland*, 1999; *Dai and Karato*, 2009b], we calibrate the polynomial for opx and cpx according to the following constraints: $\Delta H(X_{Fe} = 0.16) = 1.52$ eV for opx [*Dai and Karato*, 2009b] and $\Delta H(X_{Fe} = 0.08) = 1.87$ eV for cpx [*Xu and Shankland*, 1999]. For a comparison we plot a modified version of the conductivity models of *Xu and Shankland* [1999] for cpx and *Dai and Karato* [2009b] for opx using $\Delta H(X_{Fe})$ instead of a constant activation enthalpy (Figure 2b). The differences between the resistivity calculated considering $\Delta H(X_{Fe})$ and those determined using the original constant activation enthalpy are between 0.26 to 0.91 and −0.6 and 0.24 log units for cpx and opx, respectively. The resistivity of C2/c cpx is 0.56 log units higher that the source opx because of the strong decrease in the iron content in the new phase for z > 300 km. In the lithosphere, the resistivity decreases from 8 and 9.6–9 log units at the Moho to 2.15–2.6 and 2.6 log units at the LAB for opx and cpx, respectively.

2.3. Garnet

[24] The garnet phase is volumetrically minor in the lithospheric mantle (<6%), but accounts for 16%–30% of the sublithospheric mantle peridotite (Figure 1d). *Xu and Shankland* [1999] measured the electrical conductivity of the garnet + ilmenite phase ($X_{Fe} = 0.09$) at a pressure of 21 GPa in the range T = 1200°C–1500°C by fitting equation (1) with the following parameters: $\sigma_0 = 10^{3.35}$ S/m, $\Delta H = 1.66$ eV. The effect of iron content in garnet in the pyrope-almandine system was studied by *Romano et al.* [2006] at 10 and 19 GPa in the temperature range 300°C–1700°C. For the pressures of interest in this paper (<13.4 GPa) the activation enthalpy decreased regularly with increasing iron content [*Romano et al.*, 2006]. Similar results regarding the influence of the iron content on garnet conductivity at pressures of 18 and 23 GPa are reported by *Yoshino et al.* [2008b]. On the basis of the laboratory data presented by *Romano et al.* [2006], *Jones et al.* [2009a] defined the following equation to account for the iron content dependence in the conductivity of garnet:

$$\sigma = \sigma_0 \exp\left(\frac{-(a - bX_{Fe})}{k_B T}\right), \tag{10}$$

where $\sigma_0 = 10^{(4.26-12.26XFe)}$ S/m, a = 2.4 eV, and b = 6.

[25] *Yoshino et al.* [2008b] measured the conductivity of MORB ($X_{Fe} = 0.3$) and pyrolite majorite ($X_{Fe} = 0.07$) at pressures of 18 and 23 GPa for the temperature range 627°C–1727°C under dry conditions. They also found a conspicuous effect of iron content in the electrical conductivity of majorite garnet. The reported activation enthalpy did not show significant pressure dependence but did exhibit significant iron content variation: average of 1.47 and 1.23 eV for the pyrolite ($X_{Fe} = 0.07$) and MORB ($X_{Fe} = 0.3$) samples for T = 700°C–1500°C, respectively [*Yoshino et al.*, 2008b]. The results of these authors regarding the electrical conductivity of garnet majorite can be described by equation (10) with the following parameters: $\sigma_0 = 10^{2.83}$ S/m, a = 1.54 eV, and b = 0.87. A more recent study on a single-crystal pyrope-rich garnet ($X_{Fe} \sim 0.16$) under the conditions of 4–16 GPa and T = 600–1200°C included the effect of water content in garnet conductivity [*Dai and Karato*, 2009a]. Dai and Karato proposed a conductivity model described by equation (7) with the following parameters: $\sigma_0 = 1036(1–0.044P(GPa))$ S/m, $\Delta U = 1.32$ eV, $\Delta V = 2.5$ cm^3/mol, A = 195 S/m, $\Delta H_{wet} = 0.725$ eV and r = 0.63. The relatively high value of the activation volume implies a significant decrease of conductivity with increasing pressure under dry conditions [*Dai and Karato*, 2009a]. Such an effect of pressure on conductivity was not reported in garnet majorite by *Yoshino et al.* [2008b] and is also not present in the study by *Romano et al.* [2006], which suggests an increase in conductivity for increasing pressure (activation enthalpy < 1eV at P = 19 GPa). The latter result, however, is difficult to compare directly with the observations made by *Yoshino et al.* [2008b] and *Dai and Karato* [2009a] as the water content was not determined by *Romano et al.* [2006].

[26] Figure 2c shows the values of the conductivity models presented above for the geotherm, pressure and iron partitioning distributions with depth for our reference lithospheric column (Figure 1). At depths above the transition zone (where the garnet-majorite substitution becomes important), garnet tends to strongly partition the iron relative to other minerals. Therefore, the iron content of garnet is the highest of the upper mantle minerals in the range of bulk compositions that we are using here (Table 1). In the lithosphere, X_{Fe} varies from 0.4 to 0.23 for garnet with discontinuities of $\Delta X_{Fe} = 0.03–0.017$ at the boundaries between the mantle layers with different compositions. In the sublithospheric mantle, X_{Fe} increases almost linearly with depth from 0.25 in the vicinity of the LAB to 0.29 at the bottom of the model (Figure 1c).

[27] The model of *Xu and Shankland* [1999] is independent of pressure and composition and predicts the most resistive profile for the lithospheric mantle (i.e., T < 1315°C). The *Dai and Karato* [2009a] model is 1.57 log units less resistive than that of *Xu and Shankland* [1999], but only down to the LAB (Figure 2c). At greater depths, the pressure

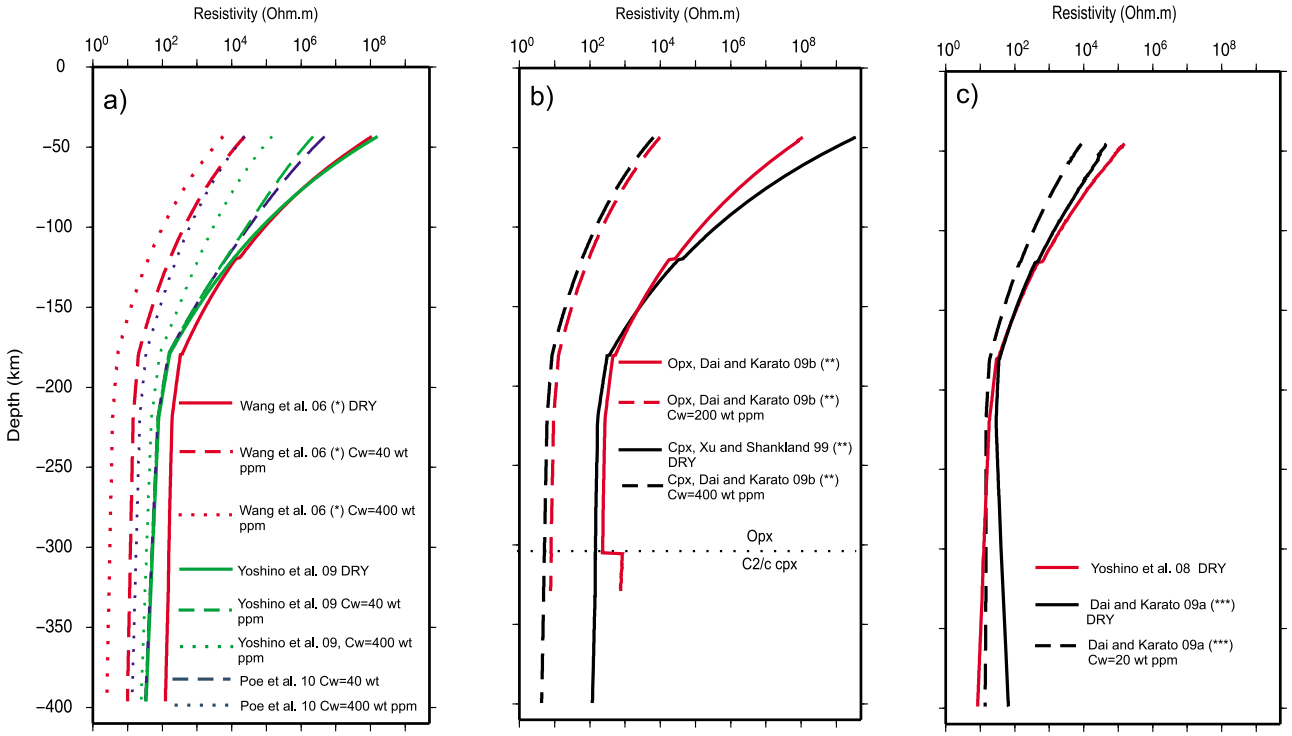

Figure 4. Comparison of different laboratory results examining the effect of water content on electrical resistivity (i.e., the proton conduction term in equation (11); see the text for further details) of (a) olivine, (b) pyroxenes, and (c) garnet. Temperature, pressure, and iron content are taken from the reference lithospheric column of Figure 1. The water content distribution with depth is assumed to be constant: for olivine, 40 wt ppm (dashed lines) and 400 wt ppm (dotted lines); for opx, 200 wt ppm (dashed red line); for cpx, 400 wt ppm (dashed black line); and for garnet, 20 wt ppm. Solid lines are dry resistivity depth profiles in all the cases. The single, double, and triple asterisks are as in Figure 2.

term makes the *Dai and Karato* [2009a] model more resistive than that of *Xu and Shankland* [1999] (by 0.76 log units at P = 13.4 GPa) because of the high and positive value of the activation volume in the work by *Dai and Karato* [2009a]. The model of *Jones et al.* [2009a] (equation (10)) predicts very low resistivity in the lithosphere (up to 5.6 log units lower with respect to the model of *Xu and Shankland* [1999]) because of its strongly compositionally dependent activation enthalpy. However, the models of *Jones et al.* [2009a] and *Xu and Shankland* [1999] show relatively close resistivity values in the sublithospheric mantle (<0.2 log units difference). The activation enthalpy is also a function of the iron content in the model of *Yoshino et al.* [2008b], but in this case, resistivity values in the lithosphere are <2 log units lower than those predicted by the *Xu and Shankland* [1999] model. In order to give an additional constraint on the X_{Fe} sensitivity in garnet conductivity, we use the activation enthalpies obtained by *Romano et al.* [2006] at P = 10 GPa to fit a fifth-order polynomial on X_{Fe}: $\Delta H(X_{Fe}) = a + b\,X_{Fe} + c\,X_{Fe}^2 + d\,X_{Fe}^3 + e\,X_{Fe}^4 + f\,X_{Fe}^5$ (Figure 3 and Table 2). The coefficients of the polynomial are calibrated according to the following constraint: $\Delta H(X_{Fe} = 0.16) = 1.55$ eV [*Dai and Karato*, 2009a]. A modified version of the *Dai and Karato* [2009a] conductivity model including the iron content–dependent enthalpy is plotted in Figure 2c. This modified version is 1.17–0.24 log units more conductive than the original model and matches relatively well (<0.54 log units difference) the resistivity values predicted by *Yoshino et al.* [2008b] in the lithosphere. These two models are less resistive than the models of *Dai and Karato* [2009a] ($X_{Fe} \sim 0.16$) and *Xu and Shankland* [1999] ($X_{Fe} = 0.09$), as might be expected because of the higher iron content of garnet in our reference column ($X_{Fe} = 0.4$–0.23). The minimum difference between the different experimental models is at the vicinity of the LAB (<0.4 log unit difference in resistivity). In the sublithospheric mantle the pressure effect makes the model of *Dai and Karato* [2009a] up to 0.9 log units (at the top of the transition zone) more resistive than *Yoshino et al.*'s [2008b] model.

2.4. Water Content

[28] From recent laboratory studies the presence of even small amounts of water (i.e., OH defects) has a considerable effect on the electrical conductivity of mantle minerals [e.g., *Wang et al.*, 1999, 2006; *Yoshino et al.*, 2009; *Poe et al.*, 2010]. However, the extent to which water affects conductivity remains controversial [e.g., *Karato and Dai*, 2009; *Yoshino*, 2010]. To quantify these differences we plot the different resistivity models, including water content dependence, under dry and wet conditions (Figure 4). The amount of water dissolved in mantle rocks is a matter of intense debate and is discussed in detail in section 4.3.2. For illustrative purposes, we will assume representative average values for each mineral on the basis of global water content

measurements in mantle rocks: 40 weight parts per million H_2O (wt ppm) for olivine, 200 wt ppm for orthopyroxene, 400 wt ppm for clinopyroxene, and 20 wt ppm for garnet [e.g., *Bell and Rossman*, 1992; *Grant et al.*, 2007; *Gose et al.*, 2008; *Peslier*, 2010]. In the case of olivine, we also consider a high water content (400 wt ppm) to analyze the sensitivity of the different proton conduction models to water content. For clinopyroxene we will assume the same water content dependence as that in the *Dai and Karato* [2009b] model for orthopyroxene, as no laboratory constraints exist for clinopyroxene.

[29] In the case of olivine, the model of *Wang et al.* [2006] shows a strong difference in resistivity between the wet (40 wt ppm) and dry models, particularly in the lithosphere (3.7–1.25 log units difference) but also in the sublithospheric mantle (1.2–1.1 log units difference). In contrast, the model of *Yoshino et al.* [2009] exhibits a wet-dry resistivity drop of 1.86 log units at the Moho, which is rapidly reduced to 0.03 log units at the LAB (Figure 4a). In Figure 4a we also plot a modified version of the model of *Yoshino et al.* [2009] in which the original proton conduction term in equation (9) has been substituted by the geometric average of the conductivities along the three crystallographic directions, according to the values determined by *Poe et al.* [2010]. This modified version yields, for 40 wt ppm, a wet to dry resistivity drop of 1.53 and 0.04 log units at the Moho and the LAB, respectively. At higher water contents (400 wt ppm) the wet-dry resistivity drop at lithospheric temperatures is similar to that of both *Poe et al.* [2010] (3.8–0.7 log units) and *Wang et al.* [2006] (4.3–1.9 log units) and is somewhat lower than that of *Yoshino et al.* [2009] (3.0–0.3 log units). In the sublithospheric mantle and for 400 wt ppm, the wet-dry resistivity drop ranges from 1.8–1.7 log units [*Wang et al.*, 2006] to 0.3–0.14 log units [*Yoshino et al.*, 2009]. Therefore, the model of *Yoshino et al.* [2009] is less sensitive to water content (except for low T and water content) than the model of *Wang et al.* [2006], which is the most sensitive. According to *Wang et al.* [2006], the proton conduction term varies strongly (up to 4.3 log units in resistivity) at low water contents (0–40 wt ppm) and only modestly (0.6 log units) at relatively high values (40–400 wt ppm). The situation is the opposite in the model of *Poe et al.* [2010], for which the most important decrease in resistivity (up to 2.3 log units) takes place at 40–400 wt ppm. The model of *Yoshino et al.* [2009] is similar to the results of *Wang et al.* [2006] in that the maximum predicted change in resistivity takes place at relatively low water content, although the differences between the resistivity drops at 0–40 wt ppm (up to 1.86 log units) and 40–400 wt ppm (up to 1.2 log units) are of lower magnitude in this case (Figure 4a).

[30] The resistivity of pyroxenes, according to the *Dai and Karato* [2009b] model, is strongly sensitive to water content and shows a wet-dry resistivity drop of 4–1.6 (opx) and 5.74–1.63 log units (cpx) for the lithosphere, and 1.4–1.5 log units in the sublithospheric mantle (opx and cpx) respectively (Figure 4b). For garnet, the resistivity decreases by up to 0.79 log units in the lithosphere in the *Dai and Karato* [2009a] model (Figure 4c).

[31] Given that the implications of the different experimental approaches used for determining the electrical effects of dissolved OH in olivine remain contentious [cf. *Karato and Dai*, 2009; *Yoshino*, 2010], we have opted for our work to use and test the results provided by all approaches.

3. Mantle Bulk Conductivity

[32] To determine comprehensively the bulk conductivity of the mantle, it is essential to select an appropriate electrical conductivity model for each constituent mineral, and to define a suitable averaging scheme or mixing rule to account for the individual contribution of each of them. Temperature is by far the most important parameter controlling the electrical conductivity of mantle minerals (Figure 2), followed by water content (Figure 4). The amount of iron is only relatively important in the case of high X_{Fe} variations, e.g., orthopyroxene at the LAB (Figure 1c). Pressure does not have an appreciable effect in the conductivity of pyroxenes [*Dai et al.*, 2006] but is relevant for olivine [*Xu et al.*, 2000] as well as for garnet [*Dai and Karato*, 2009a] in the sublithospheric mantle (T > 1300°C) (Figure 2c). As discussed by *Jones et al.* [2009a], the effect of oxygen fugacity on the conductivity of mantle minerals is only of minor importance when compared with temperature or iron content (e.g., conductivity is only a function of fO_2 to the power 1/6 for the SEO3 model in equation (5) or 2/11 for the *Du Frane et al.* [2005] model in equation (6)); therefore, we do not consider any fugacity dependence in this paper. A change in the conduction regime from small polaron to ionic conduction, related to Mg vacancies, at sublithospheric temperatures has been reported for olivine at T > 1300°C [*Schock et al.*, 1989; *Constable*, 2006; *Yoshino et al.*, 2009; *Farla et al.*, 2010] and garnet at T > 1530°C [*Yoshino et al.*, 2008b]. The ionic conduction is characterized by an activation enthalpy typically >2 eV in olivine [*Yoshino et al.*, 2009; *Farla et al.*, 2010] and >1.6 eV in garnet [*Yoshino et al.*, 2008b]. In terms of the water content dependence, at least for olivine, two different proton conduction terms have been proposed by the different laboratory groups, as described in section 2.4. The effect of these two proton conduction parameterizations on the MT responses is discussed in section 4.3.2.

[33] In this paper we adopt a model for the bulk electrical conductivity of the mantle that integrates temperature, pressure and compositional variations according to available laboratory results. The equations that we use for the conductivity of mantle minerals are

$$\sigma = \sigma_0 \exp\left(\frac{-\Delta H(X_{Fe},P)}{k_B T}\right) + \sigma_{0i} \exp\left(\frac{-\Delta H_i}{k_B T}\right) + \sigma_p,$$
$$\Delta H(X_{Fe},P) = a + bX_{Fe} + cX_{Fe}^2 + dX_{Fe}^3 + eX_{Fe}^4 + fX_{Fe}^5 + P\Delta V,$$
$$\sigma_p = f(C_w) \exp\left(\frac{-\Delta H_{wet}(C_w)}{k_B T}\right). \tag{11}$$

The first term in the first expression of equation (11) describes conduction due to small polarons, and the second term represents the contribution of Mg vacancies at high temperatures. The second expression in equation (11) is the activation enthalpy for small polaron conduction, which includes the iron content and pressure dependencies. All the experimentally derived parameters describing the conductivity model for each mineral (σ_0, σ_{0i}, a, b, c, d, e, f,

Table 3. Proton Conduction Term for the PC1 and PC2 Models[a]

PC1				PC2			
Mineral	ΔH_{wet} (eV)	log A (S/m)	r	Mineral	ΔH_0 (eV)	log A (S/m)	α
Ol[b]	0.9	3	0.62	Ol[c]	1.19	2.35	1.1
Opx[d]	0.85	2.6	0.62	Opx[e]	1.19	2.35	1.1
Cpx[f]	0.85	2.6	0.62	Cpx[e]	1.19	2.35	1.1
Gnt[g]	0.725	2.29	0.63	Gnt[e]	1.19	2.35	1.1

[a]See equation (11) and the text for further details.
[b]Olivine data are from *Wang et al.* [2006].
[c]Olivine data are from *Poe et al.* [2010].
[d]Orthopyroxene data are from *Dai and Karato* [2009b].
[e]For the pyroxenes and garnet the parameters for olivine from (4) are assumed.
[f]For the clinopyroxene the parameters for opx from (2) are assumed.
[g]Garnet data are from *Dai and Karato* [2009a].

ΔV, ΔH_i, ΔH_0) are listed in Table 2. In the third expression of equation (11) σ_p describes for the proton conduction term and integrates two possible parameterizations. The first parameterizations (hereafter PC1) are based on the experimental results from Karato's group for olivine [*Wang et al.*, 2006], orthopyroxene [*Dai and Karato*, 2009b], and garnet [*Dai and Karato*, 2009a] and are characterized by a constant value of ΔH_{wet}, and $f(C_w) = AC_w^r$. The second parameterizations (hereafter PC2) are defined by the studies of *Yoshino et al.* [2009] and *Poe et al.* [2010] of olivine conductivity: $\Delta H_{wet} = \Delta H_0 - \alpha C_w^{(1/3)}$ and $f(C_w) = AC_w$. For PC1, in the absence of laboratory data, we assume for clinopyroxene the same C_w dependence as reported for orthopyroxene by *Dai and Karato* [2009b]. For similar reasons, the proton conduction term determined for olivine by *Poe et al.* [2010] (i.e., the geometrical average along the crystallographic axes) is assumed for the pyroxenes and garnet in the PC2 model. The parameters describing both PC1 (ΔH_{wet}, A, r) and PC2 (ΔH_0, A, α) proton conduction terms are listed in Table 3.

[34] The determination of the electrical conductivity of a mantle mineral assemblage requires the averaging of the constituent minerals, taking into account their volumetric fractions and geometrical distribution. Although two-phase systems within conductive and nonconductive regimes have been broadly studied adopting simplified geometrical representations [e.g., *Spangenberg*, 1998; *Kozlovskaya and Hjelt*, 2000], these approaches are of little use in the case of the Earth's mantle, as the textural information in natural mantle rocks is only scarcely and inadequately sampled (e.g., xenoliths) and remains largely unknown. The use of averaging schemes involving no assumptions regarding the phase geometry are therefore more appropriate for determining the bulk conductivity of mantle rocks. The concept of "extremal bounds," i.e., the most extreme bounds that can possibly be obtained for a physically meaningful mixture without any textural assumptions, was first proposed by *Maxwell-Garnett* [1904] and was subsequently developed by other authors in the 1960s [*Hashin and Shtrikman*, 1963]. The Hashin-Shtrikman (HS) extremal bounds [*Hashin and Shtrikman*, 1963] are the narrowest possible limits that can be defined for a two-phase composite in the absence of geometrical information about the phases. *Berryman* [1995] derived a general form of the HS bounds for an N-phase material and particularly for the electrical conductivity:

$$\sigma_{HS}^{-} = \left(\sum_{i=1}^{N} \frac{v_i}{\sigma_i + 2\sigma_{\min}} \right)^{-1} - 2\sigma_{\min}, \tag{12}$$

where σ_{HS}^{-} is the lower bound, v_i is the volume fraction, N the number of phases and σ_{min} is the minimum conductivity of all the individual phases. The upper bound, σ_{HS}^{+}, is given by equation (12) substituting the maximum value, σ_{max}, for the minimum one. The physical meaning of σ_{HS}^{-} can be understood as a resistive matrix with noninterconnected conductive inclusions, whereas σ_{HS}^{+} would be understood as a conductive matrix with noninterconnected resistive inclusions. Series and parallel solutions provide alternative maximum and minimum conductivity estimates for a mixture of phases [*Schulgasser*, 1976, 1977]:

$$\begin{aligned} \sigma_S &= \left(\sum_{i=1}^{N} \frac{v_i}{\sigma_i} \right)^{-1}, \\ \sigma_P &= \left(\sum_{i=1}^{N} \sigma_i v_i \right), \end{aligned} \tag{13}$$

where σ_S and σ_P are the series and parallel solutions, respectively, and will also be used herein.

4. Application to the Kaapvaal Craton and the Rehoboth Terrane

[35] We model the 1-D MT responses from two case studies in southern Africa recorded as part of the Southern African Magnetotelluric Experiment (SAMTEX [*Jones et al.*, 2009b]), in two locations of different geological aged lithosphere: the Proterozoic Rehoboth Terrane (RT) and the Archean Kaapvaal Craton (KC). In contrast to the well-studied KC, the deep lithospheric structure and temperature distribution of the RT, largely hidden beneath thick Quaternary Kalahari sand cover, remain poorly defined, mainly because of data scarcity and the lack of intense exploration interest (because of the general paucity of kimberlites, particularly diamondiferous ones).

[36] The KC is subdivided into two tectonic blocks, the eastern Witwatersrand Block and the western Kimberley Block (Figure 5) [*de Wit et al.*, 1992], each with distinct geological fabrics and characteristics that attest to separate Palaeoarchean to Mesoarchean histories prior to their collision and accretion across the magnetic, and somewhat enigmatic, Colesberg Lineament (Figure 5) at about 2.9 Ga [*Schmitz et al.*, 2004].

[37] The RT was accreted to the western margin of the Kimberley Block across the magnetic Kalahari Lineament (Figure 5) by about 1750 Ma [*Jacobs et al.*, 2008]. The oldest crustal and mantle xenolith ages (from the Gibeon kimberlite field) determined for the RT infer an early Proterozoic lithospheric stabilization age [*Ziegler and Stoessel*, 1991; *Hoal et al.*, 1995]. In comparison to the eastern Kimberley Block of the KC, the RT is characterized by a present-day lithospheric thickness that is at least 40 km thinner [*Muller et al.*, 2009], a thinner highly depleted upper

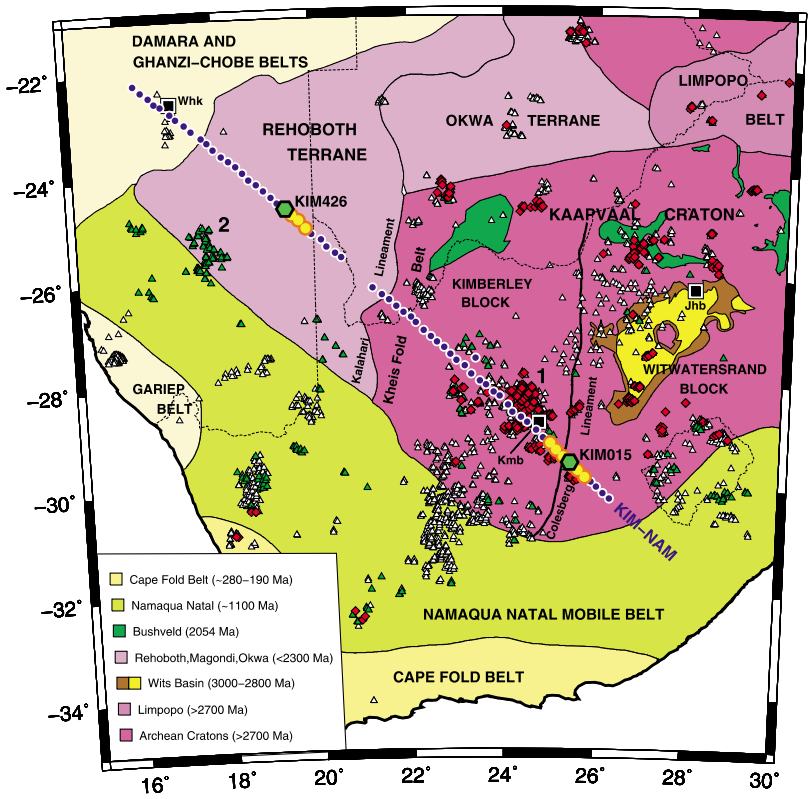

Figure 5. Simplified tectonic map of southern Africa. Shown are magnetotelluric (MT) station sites (blue dots) along profile KIM-NAM [*Muller et al.*, 2009] and kimberlite occurrences (red diamonds, known diamondiferous; green triangles, known nondiamondiferous; white triangles, unknown or unspecified in databases). The Kimberley (1) and Gibeon (2) kimberlite fields are annotated. Green octagons show the locations of the two MT sites used in this work, KIM015 in the Kaapvaal Craton and KIM426 in the Rehoboth Terrane. The sites highlighted in yellow are characterized by MT responses that are very similar to those observed at KIM015 and KIM426. Major cities (black squares) are annotated: Kimberley (Kmb), Johannesburg (Jhb), and Windhoek (Whk). Terrane boundaries are shown courtesy of S. J. Webb (University of the Witwatersrand) on the basis of the magnetic field image of southern Africa. Sources of kimberlite data are the South African Council for Geoscience numerical database, *Jelsma et al.* [2004], and S. Faure (World Kimberlites and Lamproites CONSOREM Database, version 2006-1, available at http://www.consorem.ca).

lithospheric mantle layer (117 km versus 138–167 km) [*Grütter et al.*, 1999, 2006] and a lithospheric mantle that is, on average, chemically less depleted (average Mg # for olivine equal to 91.6 in comparison with 92.6 [*Boyd et al.*, 2004]), reflecting lower degrees of partial melting during lithospheric stabilization.

[38] Southern Africa was exposed to a significant thermal event in the Cretaceous period during which most of the kimberlites found in the vicinity of the MT stations studied here were erupted (Figure 5). The majority of the kimberlites in the Kimberley area are aged between 143 and 117 Ma (group II kimberlites) or 108 and 74 Ma (group I kimberlites) [*Griffin et al.*, 2003; *Kobussen et al.*, 2008], whereas kimberlites in the Gibeon field have been dated between 75 and 65 Ma [*Spriggs*, 1988; *Allsopp et al.*, 1989; *Davies et al.*, 2001]. Mantle xenoliths entrained in these kimberlites provide evidence of significant modification and refertilization of the lower lithospheric mantle of both the KC [*Griffin et al.*, 2003; *Kobussen et al.*, 2008] and the RT [*Bell et al.*, 2003b] at the time of the Cretaceous thermalism and magmatism.

[39] The MT site modeled in the KC (site KIM015) is located in the vicinity of the boundary between the Kimberley and Witwatersrand blocks, whereas the RT site (site KIM426) lies in the middle of the terrane (Figure 5). The MT responses selected for modeling are the most isotropic 1-D responses found within each terrane along the KIM-NAM profile (Figure 5) after *Groom and Bailey* [1989] decomposition to the best regional electrical strike direction determined for each terrane at lithospheric mantle depths (see *Muller et al.* [2009] for details on the MT data processing and strike analysis and decomposition). The responses at the selected MT sites are very similar to the responses recorded at a number of adjacent sites (Figure 5), and are therefore regarded as representative of the regional structure at a one to two hundred kilometer length scale, i.e., a length scale as great as the depths of interest. It is noted that the suture between the Kimberley and Witwatersrand blocks has no obvious expression in either the MT responses recorded across the Colesberg Lineament, or in the 2-D MT model of the lithospheric mantle structure [*Muller et al.*, 2009]. The 1-D phase and apparent resistivity responses modeled

are the arithmetic and logarithmic means, respectively, of the TE and TM modes. The error bars reflect the maximum of the data processing errors, the Groom and Bailey decomposition model errors, and the departure from a 1-D assumption as defined by differences between the TM and TE modes. The fact that the data we are modeling are close to isotropic 1-D implicitly assumes that anisotropy, either because of the presence of 2-D to 3-D structures or associated with crystal preferred orientation of mantle minerals, is weak or absent.

[40] Our modeling objective is to derive a lithospheric structure beneath each MT site that is compatible with the observed elevation, surface heat flow (SHF) and xenolith data, and previous geophysical and petrological studies. As the focus of this paper is on the resistivity distribution within the mantle, we derive the crustal resistivity structure from 1-D Occam inversions [*Constable et al.*, 1987] of the MT data at crustal periods (i.e., the high frequencies) and hold the crustal structure fixed while varying the lithospheric mantle model parameters. In the mantle, the resistivity distribution is computed according to the laboratory-based mineral conductivity model presented in section 3 (i.e., equation (11)) as a function of temperature, pressure, and composition. The mantle bulk density is computed by arithmetically averaging the densities of the stable mineral phases at the pertinent temperature and pressure [*Afonso et al.*, 2008]. The predicted topography of the lithospheric columns is calculated according to crustal and mantle densities assuming local isostasy, a safe assumption given the ages of the terranes. Dynamic contributions to elevation from sublithospheric loads that could arise from convection currents are implicitly neglected [see *Fullea et al.*, 2009, Appendix C1]. One-dimensional MT responses are derived from the lithospheric resistivity-depth distributions on the basis of either the Hashin-Shtrikman (equation (12)) or series-parallel (equation (13)) solutions using *Wait*'s [1954] recursion formula for an N-layered structure.

[41] The LAB can be defined in various ways depending on the proxy to it that is assumed: seismic velocity, seismic anisotropy, electrical resistivity, composition or temperature [e.g., *Eaton et al.*, 2009]. In this work, the lithospheric mantle is characterized (1) thermally, as the portion of the mantle defined by a conductive geotherm where conduction of heat prevails over convection, and (2) compositionally, as the mantle portion characterized by a relatively depleted composition with respect to the fertile primary composition in the sublithosphere (i.e., PUM in Table 1). We thus define the LAB on the basis of thermal boundary layer (TBL) and chemical boundary layer (CBL) considerations, rather than mechanical boundary layer (MBL) ones [*Artemieva*, 2009]. A linear transition in temperature from the conductive lithospheric geotherm to the asthenospheric adiabat is imposed over a 50 km depth interval below the LAB. In this paper we extend this definition to include the electrical lithosphere and to discuss whether a correlation with the thermal and compositional characterizations can be established or not.

4.1. Elevation, Surface Heat Flow, and Radiogenic Heat Production

[42] The average surface elevation in the KC and RT (1.3 and 1.1 km, respectively), both located over the African Superswell [e.g., *Nyblade and Robinson*, 1994], is about 500 m above the average elevation for other cratonic areas. The extent to which this anomalous topography is produced by large-scale upwelling with its source at the core-mantle boundary [e.g., *Gurnis et al.*, 2000] or is supported by temperature and/or density changes in the upper mantle [e.g., *Nyblade and Sleep*, 2003; *Li and Burke*, 2006] is still a matter of debate. For the purposes of our work we assume the latter.

[43] Archean cratons are globally characterized by a relatively low SHF of 41 ± 12 mW m^{-2}, whereas for Proterozoic terranes it is on average slightly higher at 48 mW m^{-2} [*Nyblade and Pollack*, 1993]. The KC, excluding the areas of Witwatersrand Basin and the Bushveld igneous complex, is characterized by an E-W variation in SHF, with values of 38 ± 7 and 53 ± 4 mW m^{-2} in its western and eastern portions, respectively [*Jones*, 1998]. The SHF close to the MT site in the KC modeled in this work (Figure 5) is <45 mW m^{-2} [*Jones*, 1998]. In the case of the RT there are no reported SHF measurements. On the basis of the lithospheric thicknesses determined by 2-D inversion of MT data recorded along the KIM-NAM profile, *Muller et al.* [2009] estimate SHF values of 41 and 45 mW m^{-2} for the KC and RT, respectively, using geotherms defined by *Pollack and Chapman* [1977].

[44] The average crustal heat production has a large effect on the measured SHF, which is relatively insensitive to its small-scale horizontal variations [e.g., *Jaupart*, 1983]. The global average heat production for Precambrian crust is 0.77 ± 0.08 μW m^{-3}, although there are considerable variations between different geological provinces depending on their magmatic and tectonic histories [*Jaupart and Mareschal*, 2003]. The Vredefort dome, located in the Witwatersrand Basin (KC), consists of an uplifted and exposed section of supracrustal sediments and upper to lower Archean crust and thus offers us a window that can be taken as representative. A systematic survey across the Vredefort dome allowed *Nicolaysen et al.* [1981] to determine average heat production values of 1.25 μW m^{-3} for the sediments, 1.86 μW m^{-3} for the upper crust, and 1 μW m^{-3} for the middle crust. The heat production of the lower crust (i.e., at depths $z > 20$ km) within the Vredefort dome was indirectly estimated as 0.4 μW m^{-3} by Nicolaysen et al. The usual heat production values assumed in the mantle are about 0.02–0.03 μW m^{-3}, i.e., 2 orders of magnitude lower than that of the crust [e.g., *Rudnick et al.*, 1998].

4.2. Crustal and Lithospheric Structure From Previous Studies

[45] Receiver function studies of the crustal structure in southern Africa indicate a Moho depth of 34–40 km in the undisturbed Archean terranes [*Nguuri et al.*, 2001; *Nair et al.*, 2006; *Hansen et al.*, 2009], and of 45–50 km in the Proterozoic terranes and mobile belts [*Baier et al.*, 1983; *Nguuri et al.*, 2001; *Nair et al.*, 2006]. A seismic refraction study across the KC indicated that the upper crust (granitic to granodioritic composition) is about 10 km thick, with its base located at 12–18 km depth and with *P* wave velocities of 6.0–6.2 km/s [*Durrheim*, 1998]. The same study suggested a relatively low velocity lower crust (felsic granulite with a dioritic average composition) with *P* wave velocities ranging from 6.4 to 6.7 km/s. A more recent joint inversion

of *S* wave receiver functions and Rayleigh wave group velocities suggests that in the Kimberley Block (KC) the Moho depth is 36.6 ± 2.1 km and that the average *S* wave velocities (V_s) for depths >20 and >30 km are 3.8 and 3.9 km/s, respectively [*Kgaswane et al.*, 2009]. These values are the same as those of *Moorkamp et al.* [2010], who undertook a joint inversion of *P* wave receiver function, Rayleigh wave group velocities and MT data, using a genetic algorithm stochastic modeling approach, for MT data from one site close to the KC site analyzed herein, and found a two-layer crust with a Moho at around 37 km, an upper crust of 3.7–3.8 km/s, a lower crust of 3.85–4.10 km/s, and a midcrustal boundary at around 28 km. *Kgaswane et al.* [2009] interpret the relatively low V_s in terms of an intermediate to felsic lower crust, where any potential mafic component of the lower crust has been thinned or removed. The absence of a mafic lower crust is also supported by *Nair et al.* [2006] on the basis of the moderately low V_p/V_s ratio of 1.73 obtained in a receiver function study.

[46] In contrast, the crustal structure in the RT appears to be significantly different from that of the KC [e.g., *Durrheim and Mooney*, 1991]. The upper crust (V_p < 6.6 km/s) extends to a depth of 20 km, the midcrust (V_p = 6.6–7.0 km/s) ranges between 20 km and 30 km, and the lower crust (V_p = 7.0–7.6 km/s) extends to 50 km depth [*Baier et al.*, 1983, and references therein].

[47] Assuming the velocity-density relationships derived by *Christensen and Mooney* [1995], we estimate the crustal density distribution in the KC on the basis of the velocity models [i.e., *Durrheim*, 1998; *Nair et al.*, 2006; *Kgaswane et al.*, 2009] as 2730–2780 kg/m^3 in the first 12–18 km, and 2865–2955 kg/m^3 for z > 20 km. A similar estimation for the RT indicates 2920–3100 kg/m^3 for the midcrust, and 3090–3285 kg/m^3 for the lower crust.

[48] The extent of the lithosphere beneath the KC has recently been examined and discussed on the basis of various seismic studies. Body wave tomography, some surface wave studies and some *S* wave receiver functions suggest a high-velocity lid thicker than 250 km [e.g., *Zhao et al.*, 1999; *Fouch et al.*, 2004; *Freybourger et al.*, 2001; *Chevrot and Zhao*, 2007]. Other studies based on surface waves and *S* wave receiver functions find that the high-velocity lid extends to only 160–200 km, underlain by a low-velocity zone of 90–150 km thickness [*Priestley et al.*, 2006; *Li and Burke*, 2006; *Hansen et al.*, 2009]. The most recent surface wave study of the Southern African Seismic Experiment (SASE [*Carlson et al.*, 1996]) data by *Li* [2011] concludes that the LAB for the KC is, on average, 180 ± 20 km. *Li* [2011] presents evidence that the predominant kimberlite clusters on the KC erupted in regions of marked low-velocity anomalies in the cratonic lithosphere [*Li*, 2011, Figures 12 and 14], raising the question of the generic applicability of xenolith information from a cluster to the whole craton. The recent Southern African Magnetotelluric Experiment (SAMTEX [*Jones et al.*, 2009b]) 2-D magnetotelluric survey carried out across the KC and the RT shows a lithospheric thickness of 220–230 km [*Muller et al.*, 2009; *Evans et al.*, 2011] for the KC and 180 km for the RT [*Muller et al.*, 2009]. The estimate of the thickness of the lithosphere given by these authors is based on a comparison of dry olivine conductivity models and the resistivity profiles obtained by 2-D inversion of the MT data.

[49] From a compositional point of view, there is evidence for mantle chemical stratification in both the KC and the RT, as indicated by xenolith data [e.g., *Grütter et al.*, 1999, 2006; *Boyd et al.*, 2004; *Griffin et al.*, 2003; *Kobussen et al.*, 2008]. The definition of the "chemical LAB" beneath cratonic regions is a debatable point with respect to the Kaapvaal Craton, i.e., whether the base of the CBL corresponds with the base of the largely harzburgitic, highly depleted layer (with high Mg # ≈ 93.1), or the base of the underlying largely lherzolitic, refertilized and melt-metasomatized layer (with moderately lower Mg # ≈ 92.2). As indicated above, we define or regard the base of the CBL as the latter. In the case of the former definition (i.e., the base of the high Mg # layer), the CBL does not necessarily have to coincide with the base of the mantle defined on geophysical grounds, i.e., the TBL [*O'Reilly and Griffin*, 2010]. The depth of the chemical LAB in the KC, based on the depth of the highly depleted mantle layer, is 205 km for group II kimberlites (143–117 Ma) and 165 km for group I kimberlites (108–74 Ma) [*Griffin et al.*, 2003], both clusters in the Kimberley region. It is noted that all of the group II and group I kimberlites in *Griffin et al.*'s [2003] analysis are located in the 40–220 km distance range from our KC MT site KIM015 (with the exception of group II Finsch kimberlite located 280 km away from KIM015). According to Cr saturation in garnet xenocrysts, the maximum depth of the highly depleted layer is 158–167 km (group II) and 138–145 km (group I) for the Kimberley block in the Archean KC [*Grütter et al.*, 1999, 2006; *Muller et al.*, 2009]. In the RT, chemical layering is suggested by the high percentage (60%–75%) of fertile lherzolites sampled in the xenoliths from the lower part of the lithospheric mantle derived from the kimberlites in the Gibeon and Gordonia kimberlite fields [*Griffin et al.*, 2003]. The depth at which the percentage of depleted peridotite (whole rock Mg # = 92.2) sampled in the Proterozoic RT lithosphere starts to decrease downward is about 120 km according to *Griffin et al.* [2003], in agreement with the estimates from Cr saturation in garnet xenocrysts (119 km) [*Grütter et al.*, 1999, *Muller et al.*, 2009]. The vertical extent of the depleted layer in the Kimberley block of the KC appears to have been modified by chemical refertilization of the lower lithospheric mantle that took place between the eruptions of the group II kimberlites (143–117 Ma) and the group I kimberlites (108–74 Ma) [*Griffin et al.*, 2003; *Kobussen et al.*, 2008]. On the basis of group I kimberlites in the KC, the highly depleted layer in the depth range 120–165 km appears to have experienced metasomatism (decrease of the proportion of depleted harzburgites and lherzolites with respect to group II kimberlites), and in the uppermost part of the mantle (<120 km depth) relatively fertile phlogopite-rich lherzolites predominate [*Griffin et al.*, 2003].

4.3. Modelling Results

[50] Within the framework of the self-consistent LitMod modeling approach, there are a number of different variables that can potentially affect the temperature, pressure, composition and density distributions of the lithospheric mantle, and hence the predicted topography, SHF and MT responses [*Afonso et al.*, 2008; *Fullea et al.*, 2009]. However, some of these variables can be reasonably well-constrained by other observations, particularly in the crust (see section 4.2).

Table 4. Properties of the Different Crustal and Mantle Layers Used in This Study

Layer	Density[a] (kg/m^3)	Heat Production (μW/m^3)	Thermal Conductivity[b] (W/m K)	Depth of Base[c] (km)
Upper crust RT	2780	1.5	2.7	7.2
Middle upper crust RT	2820	1.86	2.7	15.2
Midcrust RT	3020	0.7	2.5	37
Lower crust RT	3200	0.4	2.1	50
Upper crust KC	2780	1.25	2.7	6.7
Middle upper crust KC	2780	1.86	2.7	15.6
Lower crust KC	2950	0.7	2.4	37.1
Depleted lithosphere RT	b	0.015	*	120
Melt-metasomatized lithosphere RT	c	0.02	*	
Fertile uppermost lithosphere KC	b	0.015	*	120
Highly depleted lithosphere KC	a	0.015	*	165
Melt-metasomatized lithosphere KC	c	0.02	*	
Sublithosphere	d	0.02	*	400

[a]Mantle densities are calculated as a function of T, P, and bulk composition. Mantle compositions a, b, c, and d correspond to average Kaapvaal harzburgite, average Kaapvaal low-T lherzolite, average Kaapvaal high-T lherzolite, and PUM M-S95 in Table 1, respectively.
[b]An asterisk (*) indicates that the thermal conductivities in the mantle vary with T and P.
[c]Blank spaces are varied depths.

Therefore, we restrict the range of possible lithospheric models for the KC and RT by fixing the crustal structure and chemical stratification in the mantle according to previous geophysical and petrological studies (Table 4), and allowing for variable LAB depth and variable mantle hydration state. Concerning the chemical stratification in the mantle in this paper, we assume (1) for the KC, a moderately fertile uppermost layer (<120 km, whole rock Mg # of 92.2), a highly depleted middle layer (120–165 km, whole rock Mg # of 93.1), and a melt-metasomatized lower layer (165 km to LAB, whole rock Mg # of 90.5), and (2) for the RT, a depleted uppermost layer (<120 km, whole rock Mg # of 92.2) and a melt-metasomatized layer (120 km to LAB, whole rock Mg # of 90.5) (Tables 1 and 4).

4.3.1. Dry Mantle

[51] One of the main conclusions of our research is that completely dry lithospheric mantle models are unable to reproduce adequately the observed MT responses. Regardless of the lithospheric structure, the slope in the predicted mantle resistivity-depth profiles, from highly resistive upper lithospheric mantle to less resistive asthenospheric mantle, is too steep (a decrease of 5–8 and 4–5 orders of magnitude in the mantle resistivities for the KC and RT, respectively; Figure 6) to match the observed MT responses for any reasonable lithospheric thickness, i.e., within the range of models that predict acceptable values for the observed topography and the SHF. In Figure 6 we show one of those dry models for both the KC and the RT. The predicted apparent resistivity is systematically higher than the observed data for periods >10 and >100 s for both the KC and the RT, respectively. The residuals of the phase misfit are strongly negative above 7 and 50 s periods, with a minimum of 10° at around 20 and 125 s for the KC and the RT, respectively. The phase residuals become strongly positive above periods of 250 s for the KC. Both the apparent resistivity and phase residuals reflect a gradient in bulk lithospheric mantle resistivity model that is too strongly negative (Figure 6).

4.3.2. Wet Mantle

[52] As discussed in section 2.4, the presence of water (i.e., OH defects) dissolved in mantle rocks can significantly enhance electrical conductivity of mantle minerals [e.g., *Karato*, 1990; *Wang et al.*, 1999, 2006; *Yoshino et al.*, 2009; *Poe et al.*, 2010]. The actual amount of water in the mantle remains a matter of intense debate and interest, as its presence dramatically affects mantle viscosity, a key parameter in geodynamic convective models. There are essentially two end-member cases in regard to defining water content in the mantle: (1) direct measurements of OH defects in mantle minerals, by means of Fourier transform infrared spectroscopy (FTIR) or secondary ion mass spectrometry (SIMS), and (2) estimates of water storage capacity based on experiments at high pressure under water-saturated conditions. In the first case it is noted that because of decompression, water can diffuse out from mantle minerals in mantle xenoliths (i.e., into grain boundaries space) on their way to the surface [*Demouchy*, 2010]. Water diffusion out may be particularly relevant for garnet and, to a lesser extent, for olivine [*Demouchy et al.*, 2006]. Therefore, measured water contents in xenolith minerals should be regarded as lower bounds on the true values. Conversely, water storage capacity or solubility reflects the maximum possible water content that a mineral, or an assemblage of minerals, can accommodate within their structures without saturating or producing a water-rich fluid or hydrous melt at a given pressure. The absorption of extra water into a xenolith rock due to reequilibration with a water saturated melt during its ascent is possible, although unlikely [e.g., *Demouchy and Mackwell*, 2006]. The actual water content distribution in the mantle must lie within the above two end-member cases, most likely closer to the minimum bound.

[53] Global measurements of water content in mantle minerals typically range from dry up to 80, 200, and 400 wt ppm for olivine, orthopyroxene, and clinopyroxene, respectively [e.g., *Grant et al.*, 2007; *Peslier*, 2010; *Peslier et al.*, 2010]. For garnet, water content varies in a wide range from >1000 wt ppm in UHP metamorphic rocks [*Xia et al.*, 2005] to <20 wt ppm in peridotites and eclogites in mantle xenoliths [*Bell and Rossman*, 1992]. The bulk water content in the upper mantle, away from subduction zones or plumes, has been estimated in 50–200 wt ppm range [*Hirschmann*, 2006, and references therein]. Interestingly, a recent compilation of water content estimates from peridotite xenoliths erupted in the KC shows a decrease in olivine water content with depth, over the depth range from P = 4.5–5.0 GPa (z = 140–160 km) to P = 7.0 GPa (z = 220 km) [*Peslier et al.*, 2010]. At P < 3.0 GPa the olivine samples in the Kaapvaal xenoliths seem to have lost their initial water content because of diffusion into their host basalts [*Peslier and Luhr*, 2006]. For pyroxenes there also appears to be a systematic variation of water content with pressure. Both clinopyroxene and orthopyroxene show a minimum in their water content at P = 2.5 GPa (z = 80 km), increasing down to 4.0–4.5 GPa (z = 120–140 km) with a plateau at around 400 and 200 wt ppm, respectively, at P > 4.5 GPa [*Peslier*, 2010]. For garnet, measurements from peridotite and eclogite rocks in xenoliths in the KC and RT reveal water contents <20 wt ppm in general, whereas Cr-poor garnet megacrysts show slightly

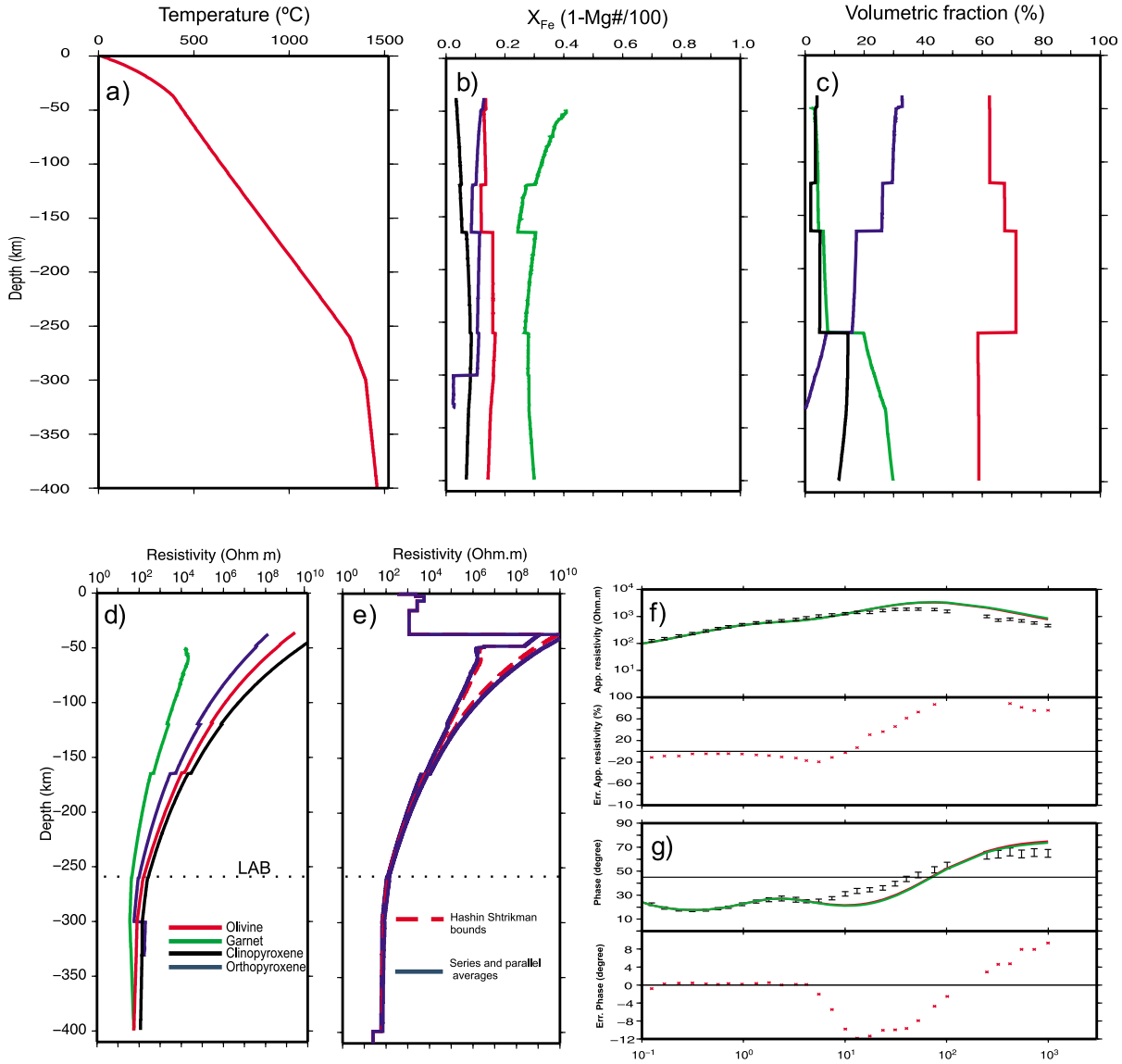

Figure 6. Dry lithospheric mantle model for (a–g) the Kaapvaal Craton at site KIM015 and (h–n) the Rehoboth terrene at site KIM426 (see location in Figure 5). The temperature (Figures 6a and 6h), the iron content (Figures 6b and 6i), the volume fractions (Figures 6c and 6j), and the electrical resistivity (Figures 6d and 6k) of the mineral phases are shown. The crustal structure and the chemical stratification in the mantle are based on previous geophysical and petrology studies (Tables 1 and 4). The predicted topography (1.25 and 1.1 km in the KC and RT, respectively) and surface heat flow (43.3 and 49.1 mW m^{-2} in the KC and RT, respectively) are compatible with the observed data (see the text for further details). The crustal resistivity structure is derived from 1-D Occam inversions of the MT data. In the mantle, the resistivity distribution is computed according to the laboratory-based mineral conductivity model of equation (11) as a function of temperature, pressure, and composition (Table 2). Figures 6e and 6l show the bulk resistivity of the mantle. The upper and lower Hashin-Shtrikman (HS) bounds (red dashed lines) and the series (upper bound) and parallel (lower bound) averages (blue solid lines) of the mineral resistivities in Figures 6d and 6k are shown. The thermal parameters used for the crust and the lithospheric mantle are listed in Table 4. The predicted MT responses are shown as red (HS minimum) and green (HS maximum) lines in the top panels of Figures 6f and 6m (apparent resistivity versus period) and Figures 6g and 6n (phase versus period). Note that given the similarities between the two responses, the HS min response (red) is almost entirely overlain by the HS max response (green). Black points in Figures 6f, 6g, 6m, and 6n show the observed MT responses with error bars that reflect the maximum of the data processing errors, the Groom and Bailey decomposition model errors, and the departure from a 1-D assumption as indicated by differences between the TM and TE modes. The bottom panels in Figures 6f and 6m and Figures 6g and 6n are the residuals (modeled minus observed) between the observed and modeled (geometrical average of HS maximum and HS minimum) responses for apparent resistivity and phases, respectively.

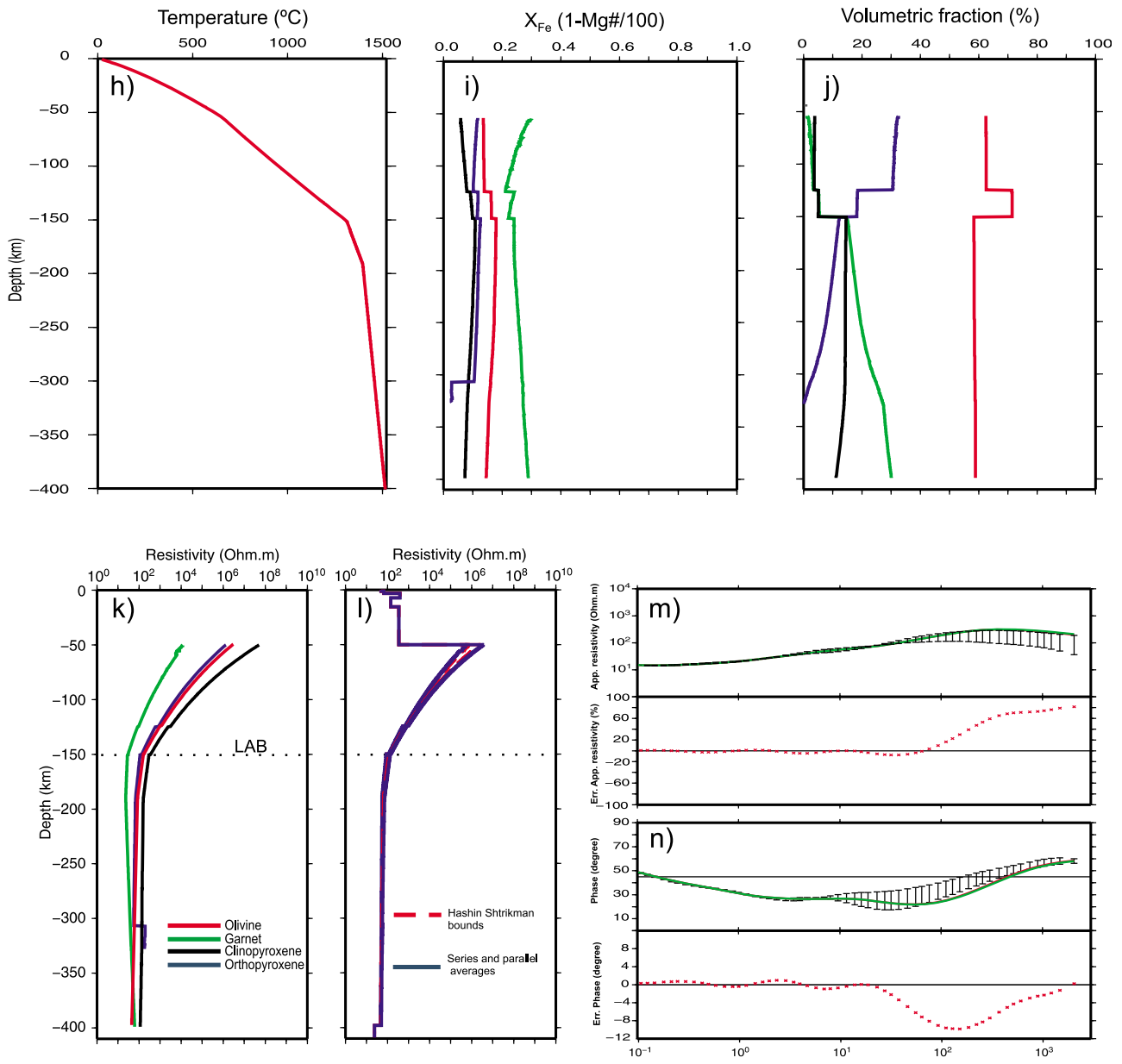

Figure 6. (continued)

higher water content values of 33 wt ppm on average [*Bell and Rossman*, 1992]. After filtering the samples with obvious inclusions from the KC, *Peslier* [2010] determined that the water content in garnet for samples coming from P > 4.5 GPa is <1 wt ppm. Figure 7a provides a summary of the water content distribution with depth for mantle minerals in xenoliths from the KC.

[54] The solubility of hydrogen (i.e., the water storage capacity) in olivine (C_{OH}^{ol}) increases systematically with increasing temperature, with increasing water fugacity and with increasing iron content [*Zhao et al.*, 2004]:

$$C_{OH}^{ol} = A f_{H_2O} \exp\left(\frac{-(\Delta E^0 + P\Delta V^0) + \gamma X_{Fe}}{R\,T}\right), \qquad (14)$$

where A = 5.62 × 10^3 wt ppm/GPa, f_{H2O} is the water fugacity (GPa), ΔE^0 = 50 kJ/mol, ΔV^0 = 10 cm^3/mol, γ = 97 kJ/mol, and R (kJ/mol K) is the universal gas constant. This solubility law assumes that f_{H2O} is for pure water calculated using the work of *Pitzer and Sterner* [1995], thus without any participation of dissolved oxides in the vapor phase (see *Bali et al.* [2008] and *Ferot and Bolfan-Casanova* [2010] for details). The water contents used in equation (14) were determined assuming the calibration of *Paterson* [1982] increased by a factor of 3.5 according to the more recent calibration of *Bell et al.* [2003a]. For the pyroxenes, the solubility of hydrogen (C_{OH}^{px}) can be described as the sum of (1) a term related to the water solubility in the Al-free pyroxenes (C_o^{px})

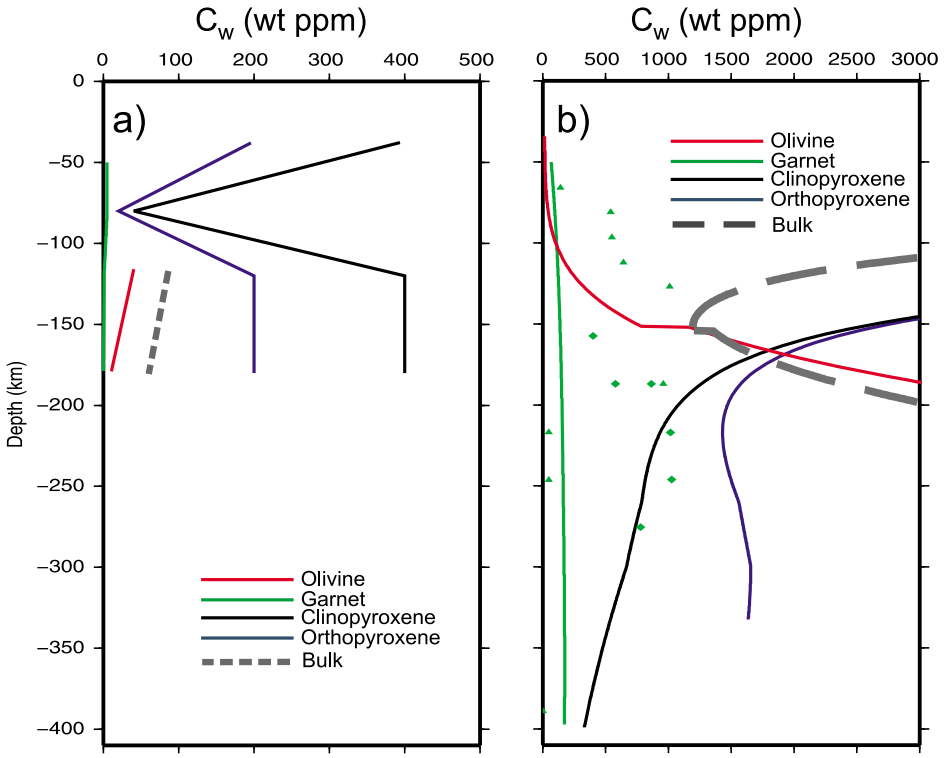

Figure 7. (a) Water content determined from xenolith measurements in the Kaapvaal after *Peslier* [2010]. (b) Water solubility in the different upper mantle minerals. For the pyroxenes aluminum-saturated conditions are assumed (see equations (14), (15), and (16) and the text for further details). Green triangles and diamonds are the experimental results for water solubility in garnet of *Withers et al.* [1998] for T = 1000°C and *Mookherjee and Karato* [2010] for T = 1100°C–1200°C, respectively. The colors of the lines in Figures 7a and 7b are as follows: red for olivine, blue for orthopyroxene, black for clinopyroxene, green for garnet, and gray (thick dashed) for the bulk rock. The absorption coefficients assumed for olivine, garnet, and the pyroxenes for both the water content measurements and the solubility models are those of *Bell et al.* [1995, 2003a].

and (2) a term accounting for the water solubility coupled to aluminum (C_{Al}^{px}) [*Mierdel et al.*, 2007]. Therefore,

$$C_{OH}^{px} = C_0^{px} + C_{Al}^{px},$$
$$C_0^{px} = A f_{H_2O} \exp\left(\frac{-(\Delta E^0 + P\Delta V^0)}{R\,T}\right), \quad (15)$$
$$C_{Al}^{px} = A_{Al} (f_{H_2O})^{1/2} \exp\left(\frac{-(\Delta E_{Al}^0 + P\Delta V_{Al}^0)}{R\,T}\right).$$

The parameters fitting the Al-free term in equation (15) have been experimentally derived for pure enstatite (opx), A = 1.35×10^2 wt ppm/GPa, $\Delta E^0 = -4.56$ kJ/mol, and $\Delta V^0 = 12.1$ cm^3/mol [*Mierdel et al.*, 2007], and for pure diopside (cpx), A = 1.85×10^2 wt ppm/GPa, $\Delta E^0 = -11.12$ kJ/mol, and $\Delta V^0 = 14.62$ cm^3/mol [*Gavrilenko*, 2008]. The Al term has been fitted to the experimental data for opx coexisting with the aluminous phase, either spinel or garnet, by *Mierdel et al.* [2007]: $A_{Al} = 4.2$ wt ppm/(GPa)$^{1/2}$, $\Delta E_{Al}^0 = -79.685$ kJ/mol, and $\Delta V_{Al}^0 = 11.3$ cm^3/mol. The absorption coefficients of *Bell et al.* [1995] were assumed to determine the OH contents in equation (14) for cpx and opx. Using equations (14) and (15), and assuming that the Al solubility term for opx can be also applied for cpx, we are able predict the OH solubility in olivine and the pyroxenes in the KC (Figure 7b). At the relevant T, P and X_{Fe} conditions for the study area, the olivine remains almost dry (<5 wt ppm) down to 60 km depth. The solubility reaches 40 wt ppm at 90 km and increases strongly at greater depths (i.e., >3000 wt ppm at z = 190 km). The Al-free water solubility of opx and cpx increases with depth to a value of 1600 and 600 wt ppm at a depths of 260 and 300 km, respectively, and then decreases steadily. If the Al term is taken into account, the water solubility in the pyroxenes in the uppermost mantle is conspicuously enhanced, being greater than 3000 wt ppm for z < 150 km. At depths > 300 km the contribution of the Al term is small, and hence the water solubility in the pyroxenes is approximately equal to that of the Al-free term. The solubility of OH in garnet remains controversial, particularly at P > 7 GPa. The solubility of water in natural pyrope was studied by *Lu and Keppler* [1997] at T = 1000°C and assuming the oxygen fugacity of the Ni-NiO buffer. Lu and Keppler give the following expression:

$$C_{OH}^{gt} = A (f_{H_2O})^{1/2} \exp\left(\frac{-(\Delta E^0 + P\Delta V^0)}{R\,T}\right), \quad (16)$$

where A = 18.09 wt ppm/(GPa)$^{1/2}$, $\Delta E^0 = -14$ kJ/mol, $\Delta V^0 = 5.71$ cm^3/mol. Note that the original value of A given

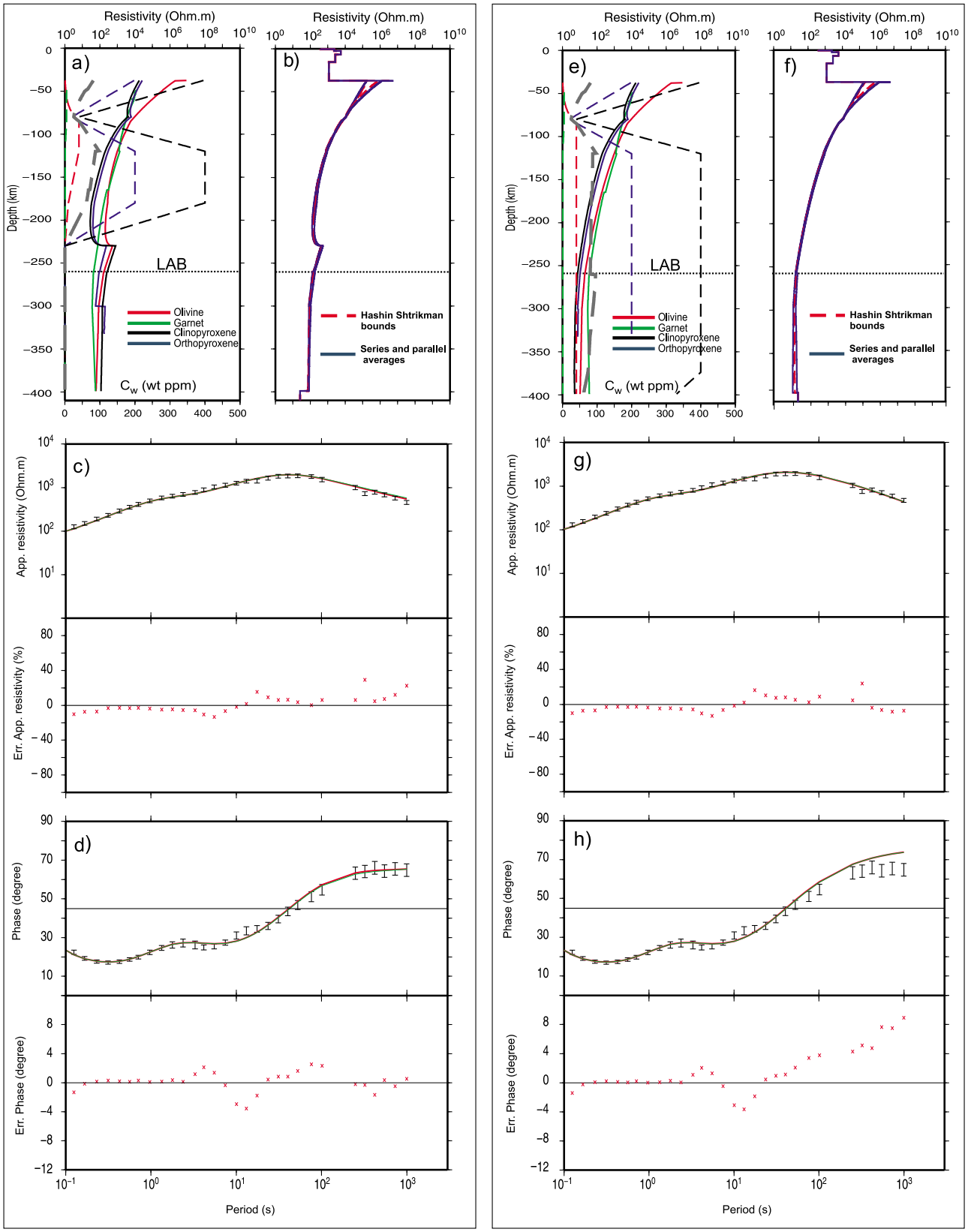
Resistivity (Ohm.m)
a)
b)
e)
f)
Depth (km)
LAB
Olivine
Garnet
Clinopyroxene
Orthopyroxene
C_w (wt ppm)
Hashin Shtrikman bounds
Series and parallel averages
c)
g)
App. resistivity (Ohm.m)
Err. App. resistivity (%)
d)
h)
Phase (degree)
Err. Phase (degree)
Period (s)

Figure 8

by *Lu and Keppler* [1997] (67.9 wt ppm/$(GPa)^{1/2}$), strictly valid only for T = 1000°C, has been appropriately changed to include the enthalpy of the reaction in equation (16) and, therefore, make the formula suitable for calculations at various temperatures. The parameters in equation (16) are computed for water contents measured using the calibration of *Bell et al.* [1995]. The OH solubility in garnet, according to equation (16) at the relevant T and P conditions in the KC, ranges from 70 wt ppm to 190 wt ppm and is plotted in Figure 7b. An experimental study on pyrope garnets at T = 1000°C and P = 2–13 GPa determined that, in the presence of excess SiO_2, the water solubility of garnet increases down to 5 GPa (z = 160 km) to values in excess of 1000 wt ppm, and then decreases to below the detection limit for P > 7 GPa (z = 215 km) [*Withers et al.*, 1998]. However, a recent study on the solubility of pyrope-rich garnet at T = 1100–1200°C and P = 5–9 GPa shows water solubility values in excess of 1000 wt ppm for P > 7 GPa [*Mookherjee and Karato*, 2010]. The value of the solubility according to *Withers et al.* [1998] is generally above that predicted by *Lu and Keppler* [1997] except for z > 215 km. The experimental results of *Mookherjee and Karato* [2010] indicate a higher solubility than that of *Lu and Keppler* [1997] for the whole lithospheric and sublithospheric mantle (Figure 7b). The bulk water solubility shows a minimum of 750 wt ppm at a depth of about 160 km. For depths >220 km, olivine becomes the strongest potential water host because of its high water solubility in comparison with that of the pyroxenes or garnet (Figure 7b).

[55] The water content in the uppermost mantle should be bound on the low side by the measured water content in rock samples, and on the high side by the water solubility, and lie most likely close to the xenolith measurements. The reliable, high-quality MT broadband data used in this study provides data at periods of <2000 s, which lack penetration to the deep sublithospheric mantle. Therefore, the question of whether the sublithospheric mantle is wet or dry is beyond of the scope of this paper. The predicted MT responses are highly dependent on the proton conduction term assumed. In this paper we consider two proton conduction parameterizations based on different experimental results: PC1 and PC2 (see section 3). The electrical asthenosphere has often been defined as a region of low resistivity, typically 5–20 Ωm, and often interpreted as a region of partial melt [e.g., *Jones*, 1999]. However, regardless of the proton conduction term assumed, our results are suggestive of relatively dry lithospheric and sublithospheric mantle in the vicinity of the LAB (Figures 8 and 9), which would be less prone to melting at the relevant T and P conditions. In our preferred models we image a region of relatively low resistivity (minimum values of 100–300 and 20–100 Ωm for the KC and the RT, respectively) that is the result of the combination primarily of two different factors: the temperature profile (i.e., the thermal LAB) and the water content variation with depth.

4.3.3. PC1 Model

[56] The water content of the different mantle minerals derived from measurements in xenoliths [*Peslier*, 2010] indicates a bulk C_w < 100 wt ppm (Figure 7a), assuming the modal proportions for each mineral phase shown in Figures 6c and 6j. There are no constraints from xenoliths regarding water content in olivine for z < 120 km in the KC, and the water solubility studies point to a rather dry uppermost mantle olivine (i.e., < 5 wt ppm at z = 60 km; see Figure 7b). At depths > 180 km there are no xenolith data available to constrain the water content in any of the mantle minerals.

[57] Interestingly, our results assuming PC1 (Figure 8) favor models in which the uppermost, relatively depleted lithospheric mantle is wetter than the underlying, fertile, and melt-metasomatized lithospheric mantle layer (Figures 8a–8d). In particular, the lower bound of a relatively low resistivity region is marked by a sudden increase of resistivity controlled by the depth of the wet-dry transition, z_{wd}. This feature is superimposed on the general trend regulated by the temperature, i.e., the depth of the thermal boundary layer, z_{LAB}. Models in which the lowermost lithospheric mantle and upper asthenospheric mantle in the vicinity of the LAB are wet, or at least as wet as the uppermost mantle (according to xenolith data, around 80 wt ppm bulk water concentration), predict higher phase values than present in the observed MT responses at periods >100 s (Figure 8h) and provide a poorer fit to the observations than the water content model of Figure 8a.

4.3.4. PC2 Model

[58] In PC2 the electrical resistivity is less strongly reduced by the presence of water than in PC1. If PC2 is assumed, the water content derived from xenolith data in the KC [*Peslier*, 2010] is too low to account for the observed MT responses, and the predicted responses are very similar to that of a dry model (Figure 6). The bulk water content required in the lithosphere, to obtain a reasonable fit to the observed MT data using PC2, is about 200–400 wt ppm (Figures 9a–9d). As in the case of PC1, a model in which the sublithospheric mantle remains as wet as the lithosphere in the vicinity of the LAB fails to explain the observed long-period phase values according to PC2 (Figures 9e–9h).

Figure 8. (a and e) Resistivity and water content versus depth profiles for the Kaapvaal Craton at site KIM015 (see location in Figure 5) for the different mantle minerals assuming the proton conduction term PC1 (equation (11) and Tables 2 and 3). The thick gray dashed line is the bulk water content. Note that models 1 (left) and 2 (right) correspond with different water content concentration. (b and f) Bulk resistivity depth profile including the crust. In the mantle, the upper and lower Hashin-Shtrikman bounds (red dashed lines) and the series (upper bound) and parallel (lower bound) averages (blue solid lines) are shown for the mantle mineral assemblage (Figure 6c). The predicted MT responses are shown as red (HS minimum) and green (HS maximum) lines in the top panels of Figures 8c, 8d, 8g, and 8h for (c, g) apparent resistivity versus period and (d, h) phase versus period. Note that given the similarities between the two responses, the HS min response (red) is almost entirely overlain by the HS max response (green). Black points represent the observed values. The bottom panels in Figures 8c and 8g and Figures 8d and 8h are the residuals (modeled minus observed) of the apparent resistivity and phase responses, respectively. The depth of the lithosphere-asthenosphere boundary (LAB) is 260 km, and the predicted topography (for local isostasy) and surface heat flow are 1250 m and 43.3 mW m^{-2}, respectively.

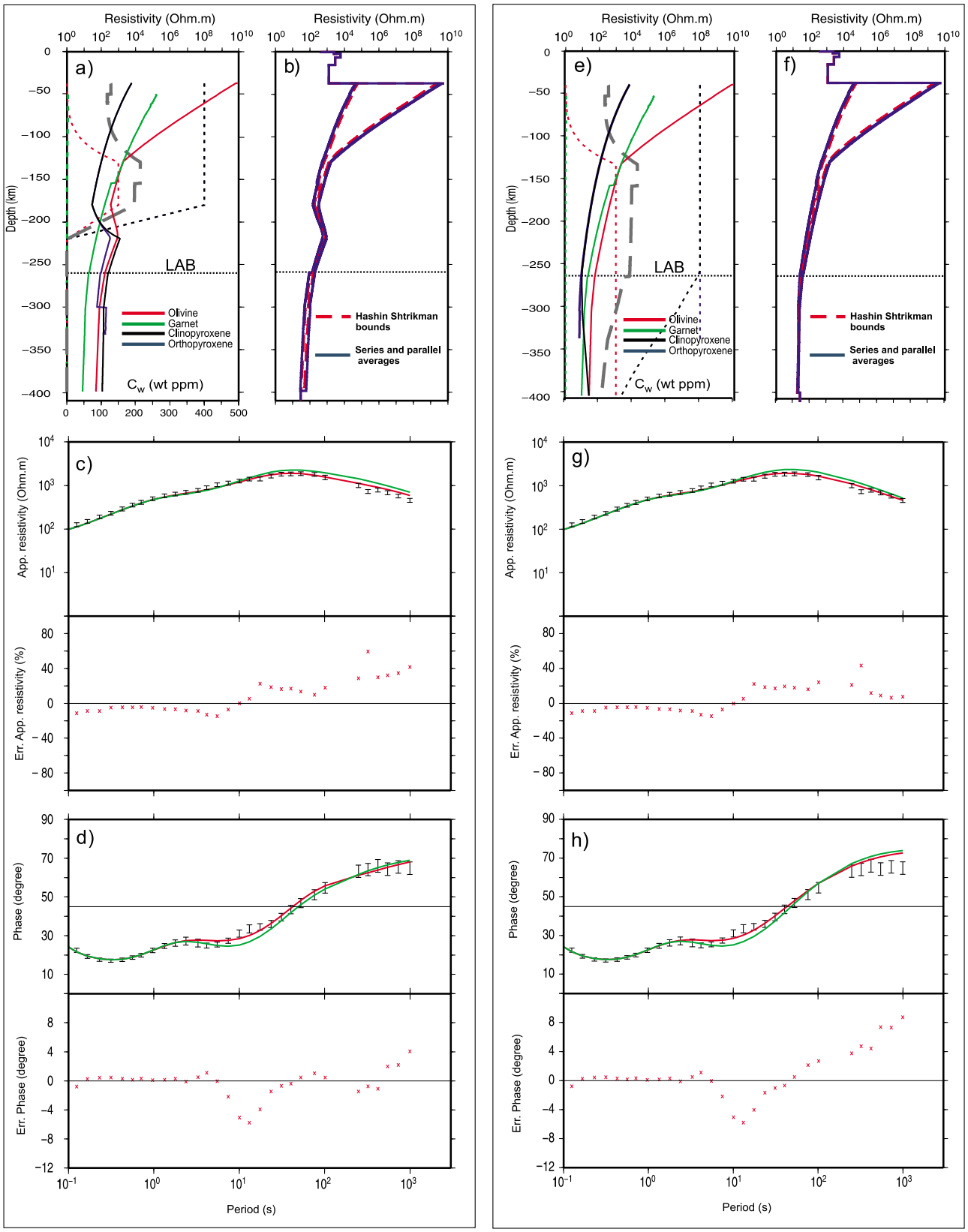
Resistivity (Ohm.m)
a)
b)
e)
f)
Depth (km)
LAB
Olivine
Garnet
Clinopyroxene
Orthopyroxene
C_w (wt ppm)
Hashin Shtrikman bounds
Series and parallel averages
c)
g)
App. resistivity (Ohm.m)
Err. App. resistivity (%)
d)
h)
Phase (degree)
Err. Phase (degree)
Period (s)

Figure 9

There is a conspicuous difference between the maximum and minimum HS bounds for PC2 because the amount of water that can be dissolved in olivine is limited by the experimental solubility, at least in the first 100 km of the mantle (Figure 7b). That makes olivine substantially drier, i.e., more resistive, than the other minerals. Particularly the pyroxenes can accommodate several hundreds wt ppm of water in the uppermost mantle (Figure 7b). Therefore, most of the water needs to be hosted in the pyroxenes (up to 800 wt ppm) in order to achieve the bulk water content required to reduce the bulk resistivity and fit the MT data. The difference between the minimum and maximum HS bounds translates into quite different MT responses in the case of PC2. The maximum bound (i.e., olivine accounting for most of the bulk resistivity) is, in general, too resistive to fit the MT data, whereas the minimum bound (essentially controlled by orthopyroxene) fits the apparent resistivity and phase similar to PC1 (Figures 8c, 8d, 8g, and 8h). The geometrical average of the HS bounds would predict, in general, too high an apparent resistivity between 10 and 100 s periods and too low a phase response around 10 s (Figures 9c, 9d, 9h, and 9h).

4.3.5. Sensitivity Tests

[59] The predicted MT responses are sensitive to both temperature and water content distributions with depth whereas the predicted topography and SHF depend only on the depth of the thermal LAB (assuming constant values for the thermal parameters and the crustal density; Table 4). The resistivities of the mantle mineral constituents assuming PC1 are not very different, i.e., <1 log unit of difference among them, except for the upper 80 km where the water solubility in olivine is almost negligible and its resistivity is higher than that of the rest of the minerals. Therefore, the minimum and maximum HS bounds for the bulk resistivity are nearly coincident for most of the depth range (Figures 8b and 8f). Furthermore, the difference between the HS bounds in the upper 80 km due to the dry olivine does not significantly affect the predicted MT responses (Figures 8c, 8d, 8g, and 8h). In Figure 10 we show a set of lithospheric models assuming PC1 and the water content measurements from KC mantle xenoliths (Figure 7a) that fit the measured MT responses in the KC and RT within the error bars, whenever possible, for different z_{wd} and z_{LAB} values. For our preferred model in the KC, the thermal LAB is at a depth of 260 ± 20 km, and average predicted topography and SHF are 1250 m and 43.3 mW m^{-2}, respectively (Figure 10a). In regard to the depth of the wet-dry transition, our preferred model shows a value of 230 ± 20 km (Figure 10d). We assume the water content derived from mantle xenoliths in Kaapvaal as a reasonable estimate in the RT in the absence of direct measurements in xenoliths (Figure 7a). We find that the best fitting model in the RT, according to PC1, is characterized by a thermal LAB and wet-dry transition depth of 150 ± 10 and 155 ± 15 km, respectively, with predicted topography and SHF values of 1100 m and 49.1 mW m^{-2}, respectively (Figures 10g and 10j). A variation of ±20 km in z_{LAB} changes the predicted topography and SHF by ±100 and ±200 m and ±0.6 and ±1.6 mW m^{-2} in the KC and RT, respectively. A sensitivity test on other model parameters is shown in Table 5.

[60] A similar analysis for PC2 is shown in Figure 11. For our preferred lithospheric model in the KC the LAB depth is 230 km. A thinner lithosphere (i.e., z_{LAB} = 200 km) predicts too high long-period phases, and a thicker lithosphere (i.e., z_{LAB} = 260 km) gives too elevated apparent resistivities (Figures 11a–11c). The effect of water content for PC2 is more subtle than for PC1. A bulk water content 2–4 times higher than that derived from xenoliths (Figure 7a) yet still within the bounds imposed by solubility (Figure 7b) is required to fit the data (Figures 11d–11f). In the KC, models in which C_w starts to decrease at around 170 km depth are preferred, i.e., close to the chemical boundary between the highly depleted and the fertile melt-metasomatized mantle according to xenoliths (Figures 11g–11i). The situation is similar in the RT, where the preferred model assuming PC2 shows an LAB depth of 165 km and requires relatively high bulk water content (few hundreds of wt ppm), as in the case of the KC (Figures 11j–11r). Our modeling for the RT favors models in which C_w decreases in the vicinity of the LAB, i.e., in the depth range 140–170 km (Figures 11p–11r).

5. Discussion

[61] Dry lithospheric mantle models are unable to reproduce the measured MT responses in both the KC and the RT (Figure 6). This discrepancy between lithospheric electrical conductivity models based on experimental laboratory studies for dry minerals and the values obtained from MT and deep geomagnetic soundings has been described by several authors for different regions [e.g., *Lizarralde et al.*, 1995; *Gatzemeier and Moorkamp*, 2005; *Kelbert et al.*, 2009; *Evans et al.*, 2011]. Excluding other possible factors (e.g., partial melt or interconnected highly conductive phases), the presence of some amount of water in the lithospheric-mantle can reasonably explain the observed MT data in the Precambrian terranes analyzed here. The amount of water required to fit the observations varies depending on the proton conduction model considered and is close to measurements made on xenoliths [e.g., *Peslier et al.*, 2010] in the case of PC1 (Figure 8a).

[62] Thermobarometry data from mantle xenoliths offer us information about the paleothermal and compositional structure of the mantle at the time of their entrainment in the

Figure 9. (a and e) Resistivity and water content versus depth profiles for the Kaapvaal Craton at site KIM015 (see location in Figure 5) for the different mantle minerals assuming the proton conduction term PC2 (equation (11) and Tables 2 and 3). The thick gray dotted line is the bulk water content. Note that models 1 (left) and 2 (right) correspond with different water content concentration. (b and f) Bulk resistivity depth profile including the crust. In the mantle, the upper and lower Hashin-Shtrikman bounds (red dashed lines) and the series (upper bound) and parallel (lower bound) averages (blue solid lines) are shown for the mantle mineral assemblage (Figure 6c). The predicted MT responses are shown as red (HS minimum) and green (HS maximum) lines in the top panels of Figures 9c, 9d, 9g, and 9h for (c and g) apparent resistivity versus period and (d and h) phase versus period. Black points represent the observed values. The bottom panels in Figures 9c and 9g and Figures 9d and 9h are the residuals (modeled minus observed) of the apparent resistivity and phase responses, respectively.

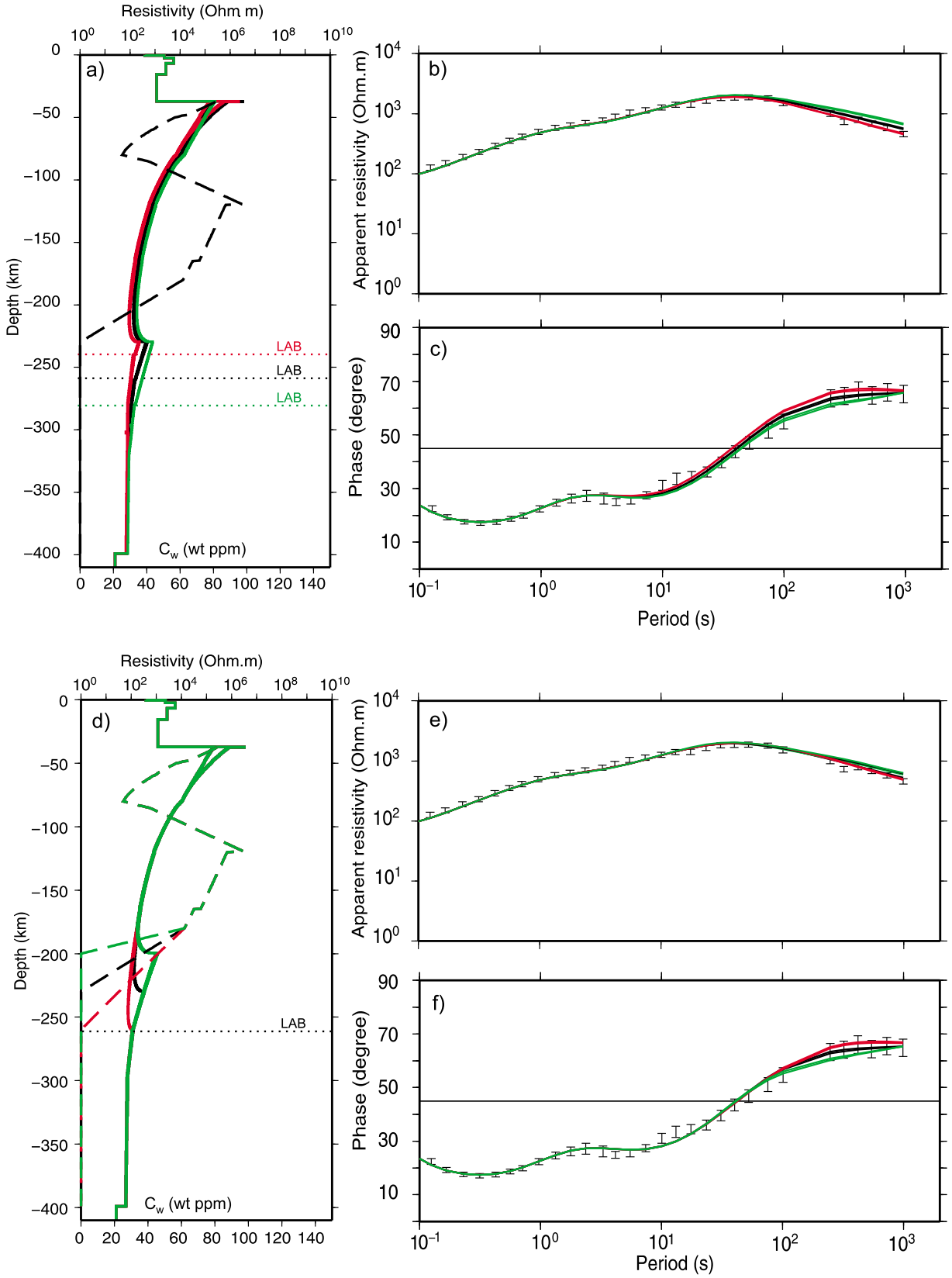
Resistivity (Ohm m)
a)
b)
c)
Depth (km)
LAB
LAB
LAB
C_w (wt ppm)
Apparent resistivity (Ohm.m)
Phase (degree)
Period (s)
Resistivity (Ohm.m)
d)
e)
f)
Depth (km)
LAB
C_w (wt ppm)
Apparent resistivity (Ohm.m)
Phase (degree)
Period (s)

Figure 10

Table 5. Sensitivity of the Calculated Topography and Surface Heat Flow (SHF) to Model Parameters[a]

	Kaapvaal Craton		Rehoboth Terrane	
	ΔE_{calc} (m)	ΔSHF_{calc} (mW m^{-2})	ΔE_{calc} (m)	ΔSHF_{calc} (mW m^{-2})
$\Delta A_c = \pm 0.15$ μW m^{-3}	±100	±3.1	±60	±3.3
$\Delta \rho_c = \pm 35$ kg m^{-3}	±425	-	±550	-
$\Delta z_c = \pm 2$ km	±300	±0.3	±70	±0.1
$\Delta z_{LAB} = \pm 20$ km	±130	±0.6	±200	±1.6

[a] E_{calc} and SHF_{calc} are the predicted topography and SHF, respectively. A_c is the crustal heat production, ρ_c is the average crustal density, and z_c and z_{LAB} are the Moho and thermal lithosphere-asthenosphere boundary depths, respectively.

host magma. These conditions do not coincide necessarily with the present-day structure, as imaged by geophysical studies. The kimberlites from groups II and I in the KC define, assuming steady state thermal conditions, paleogeotherms characterized by thermal LAB depths of 250–260 and 200–220 km at 120 and 90 Ma, respectively [*Griffin et al.*, 2003] (Figure 12). From a compositional point of view, the lowermost portion of the highly depleted layer, below about 165 km depth, was melt-metasomatized and replaced by (or enriched to form) more fertile lithospheric mantle (including many sheared lherzolites) because of a thermal or magmatic event that took place between circa 120 and 90 Ma [*Griffin et al.*, 2003; *Kobussen et al.*, 2008]. This process was accompanied by significant metasomatism in the depleted mantle induced by infiltrating fluid-rich magmas: xenoliths from younger group I kimberlites sample a layer (<165 km depth) of depleted harzburgites and lherzolites with common inclusions of hydrous phases like phlogopite and amphibole, and a shallow uppermost mantle (<120 km) dominated by more fertile phlogopite-bearing lherzolites [*Griffin et al.*, 2003]. Regardless of the proton conduction model assumed, our results suggest that the uppermost depleted part of the lithosphere contains more water that the lowermost melt-metasomatized and refertilized lithosphere. Furthermore, the depth of the electrical LAB, if it were to be interpreted as corresponding with the cusp observed in the resistivity depth profiles for wet-dry models, is controlled by the distribution of water within the lithosphere, and the absolute value of the resistivity profile is determined by water content and temperature (i.e., the depth of the thermal LAB). For models in which the upper and lower lithospheric mantle are either both wet or dry, the electrical LAB, if interpreted as the depth at which the transition to a low-resistivity gradient occurs, would correspond with the thermal LAB.

[63] Our results in the KC favor a thermal LAB depth of 230–260 km with a progressively dryer melt-metasomatized layer (>165 km) below a rehydrated and metasomatized depleted mantle layer (Figure 12). The question of whether or not the sublithospheric mantle below the KC and RT remains dry cannot be resolved in this work because of the lack of very long period MT data that are required for deeper penetration. The lithospheric thickness in the KC derived in this study is compatible, within error, with previous geophysical studies: body wave tomography, surface waves and *S* wave receiver functions [e.g., *Zhao et al.*, 1999; *Fouch et al.*, 2004; *Freybourger et al.*, 2001; *Chevrot and Zhao* 2007] and 2-D MT modeling [*Muller et al.*, 2009; *Evans et al.*, 2011] studies. The ~250 km depth thermal LAB differs significantly from the petrological LAB as defined by the base of a depleted mantle layer (~165 km) which might represent an upper level of melt penetration and accumulation within the lower lithosphere [*O'Reilly and Griffin*, 2010].

[64] Similar results regarding the water content of the cratonic lithosphere in the Archean Superior Province (Canadian Shield) were obtained by *Hirth et al.* [2000] on the basis of a comparison of conductivity-depth profiles derived from MT and geomagnetic soundings, and predicted by laboratory results. Their conclusion was that cratonic lithosphere is well described by dry olivine conductivity in the depth range of 150–250 km. In regard to the KC, the resolution tests carried out by *Evans et al.* [2011] on SAMTEX data concluded that 2-D MT modeling alone is not sufficient to discriminate between dry and slightly wet lowermost lithospheric mantle in that terrane. In contrast, the oceanic lithosphere beneath the northeastern Pacific was proposed to be relatively wet (at least 100 wt ppm) at depths of 200 km according to long-period MT data [*Lizarralde et al.*, 1995]. One of the main potential consequences of a dry cratonic lower lithospheric mantle, as imaged in our models, is that mantle viscosity is dramatically increased with respect to the possibly wetter and warmer surrounding mantle at similar depths. That, in turn, would prevent the cold, depleted and viscous cratonic roots from being eroded by convection processes over long-term geological time scales [e.g., *Li et al.*, 2008]. The present-day geotherm in the KC arising from our modeling (thermal LAB ~245 km) is slightly colder than the paleogeotherm sampled by xenoliths at 90 Ma, yet warmer that the 120 Ma paleogeotherm (Figure 12). This may be suggestive of a thermal relaxation process by which the lithospheric mantle in the KC would be recovering its earlier geotherm (as sampled by

Figure 10. Sensitivity tests for the MT data for (a–f) the Kaapvaal Craton at site KIM015 and (g–l) the Rehoboth Terrane at site KIM426 (see location in Figure 5) assuming the proton conduction model PC1 (equation (11) and Tables 2 and 3). Bulk resistivity depth profile including the crust (Figures 10a, 10d, 10g, and 10j). In the mantle, the upper and lower Hashin-Shtrikman bounds of the mantle mineral resistivity are shown. In Figures 10a and 10g the colors correspond to different LAB depth values: red is 230 km (Figure 10a) and 140 km (Figure 10g), black is 260 km (Figure 10a) and 150 km (Figure 10g), and green is 290 km (Figure 10a) and 160 km (Figure 10g). The black dashed line is the bulk water content. Figures 10d and 10j are the same as Figures 10a and 10g, but the colors show different water content distributions with depth. The predicted apparent resistivity (Figures 10b, 10e, 10h, and 10k) and phase (Figures 10c, 10f, 10i, and 10l) for the geometrical average of the Hashin-Shtrikman bounds of the resistivity profiles in Figures 10a, 10d, 10g, and 10j are also shown in Figures 10b, 10c, 10e, 10f, 10h, 10i, 10k, and 10l. Black points in Figures 10b, 10c, 10e, 10f, 10h, 10i, 10k, and 10l represent the observed values with the associated error bars as described in Figure 6. The colors in Figures 10b, 10c, 10e, 10f, 10h, 10i, 10k, and 10l represent the MT responses for the different resistivity depth profiles in Figures 10a, 10c, 10g, and 10j.

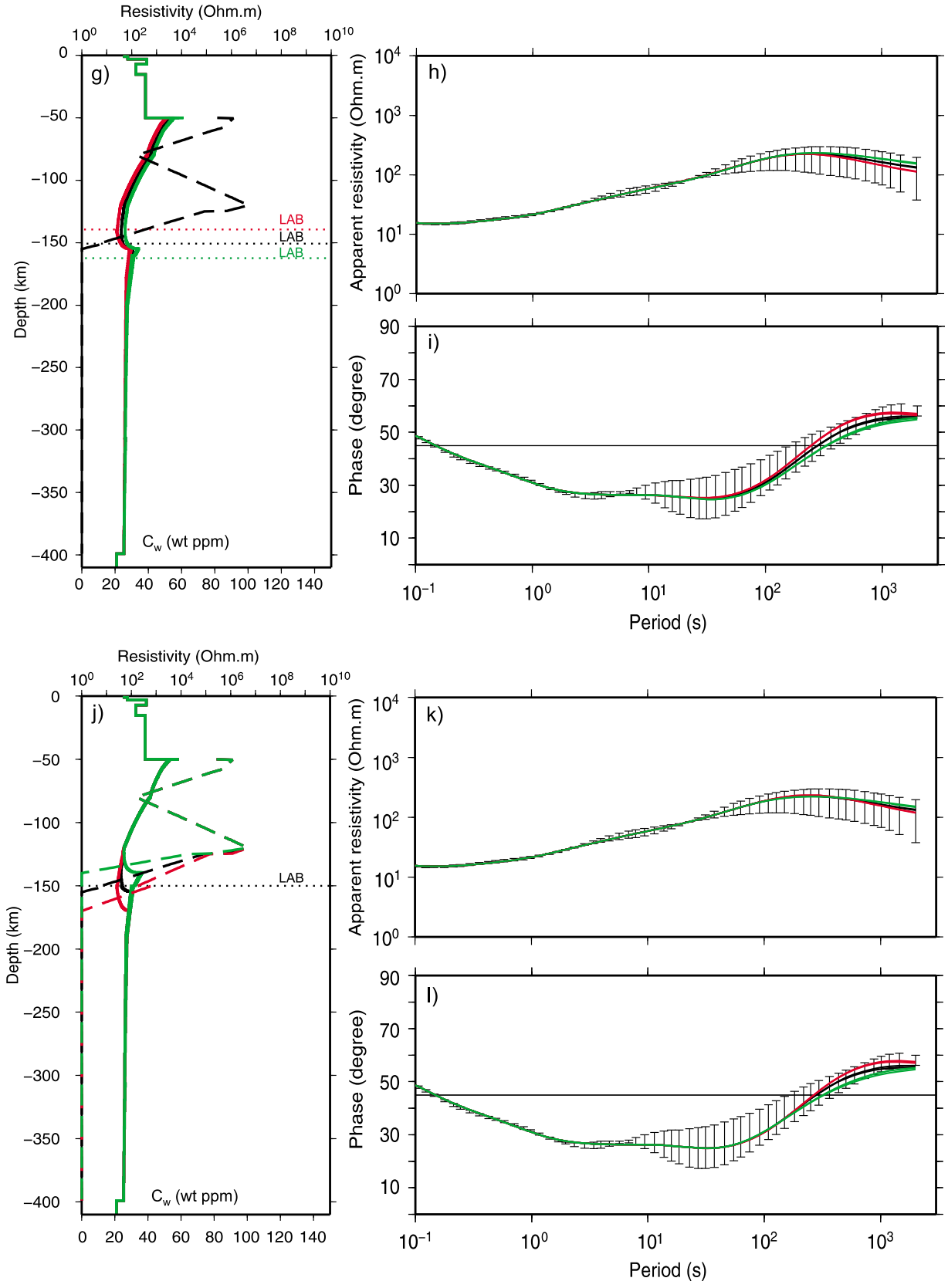

Figure 10. (continued)

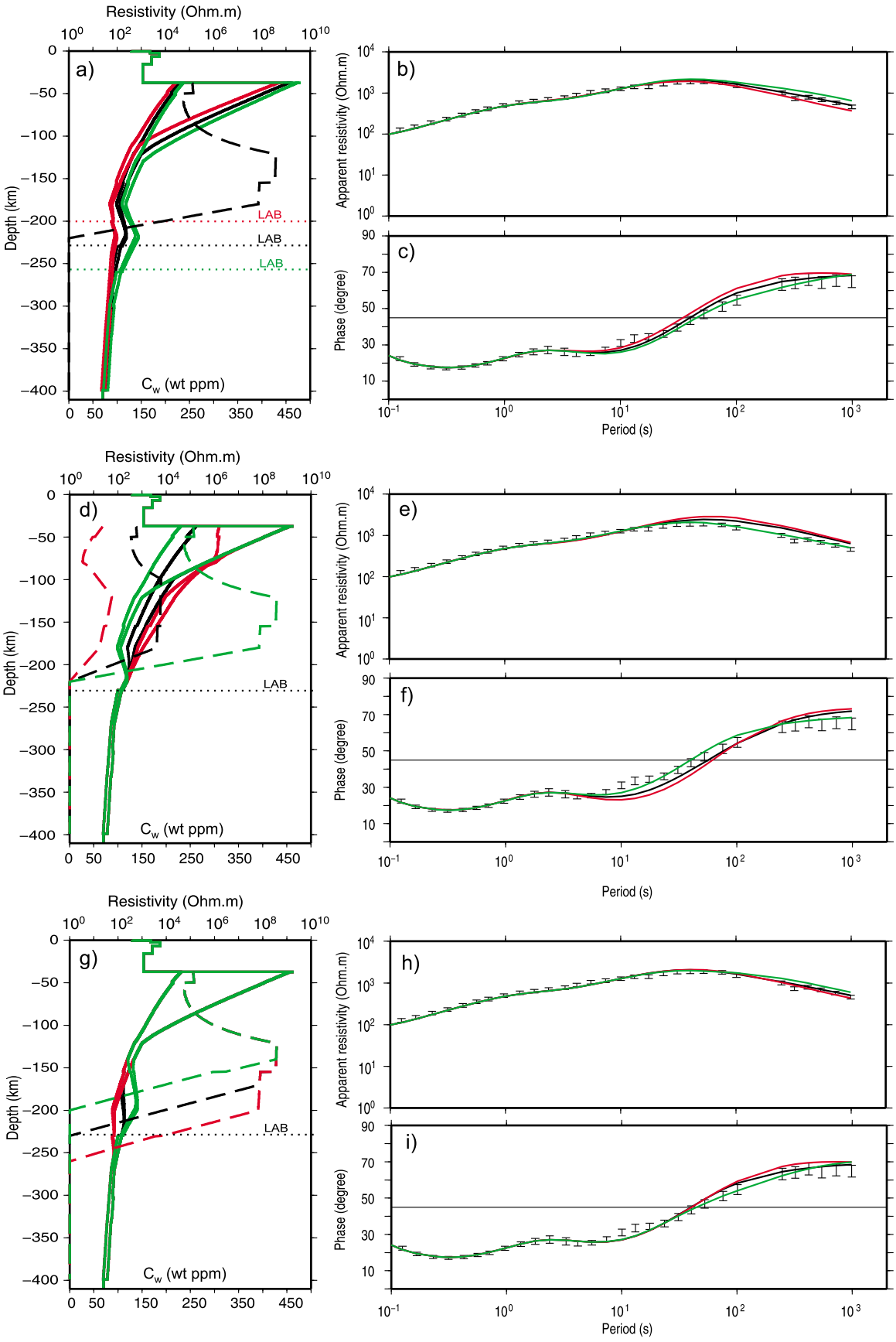
Resistivity (Ohm.m)
a)
b)
c)
d)
e)
f)
g)
h)
i)
Depth (km)
LAB
C_w (wt ppm)
Apparent resistivity (Ohm.m)
Phase (degree)
Period (s)

Figure 11

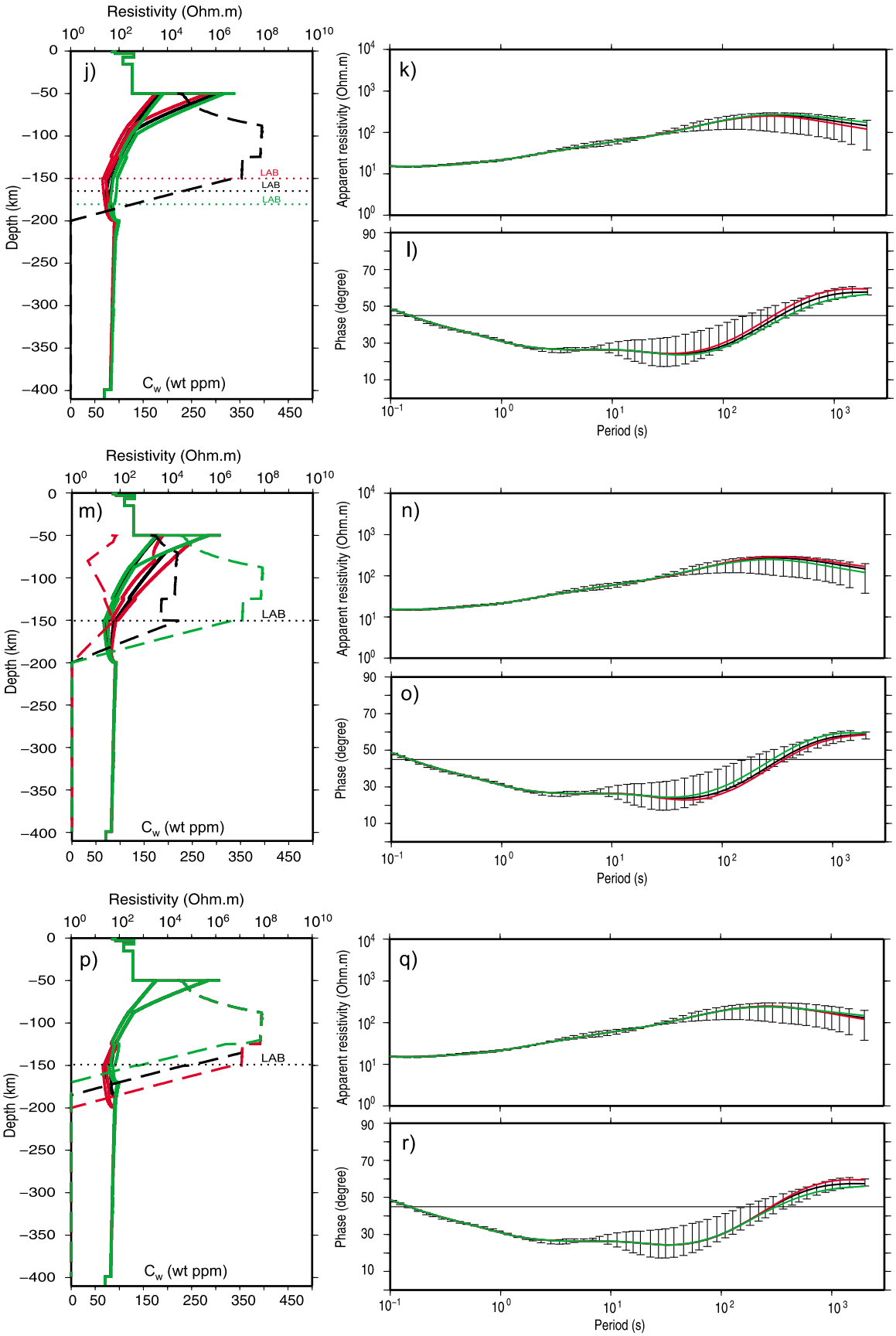

Figure 11. (continued)

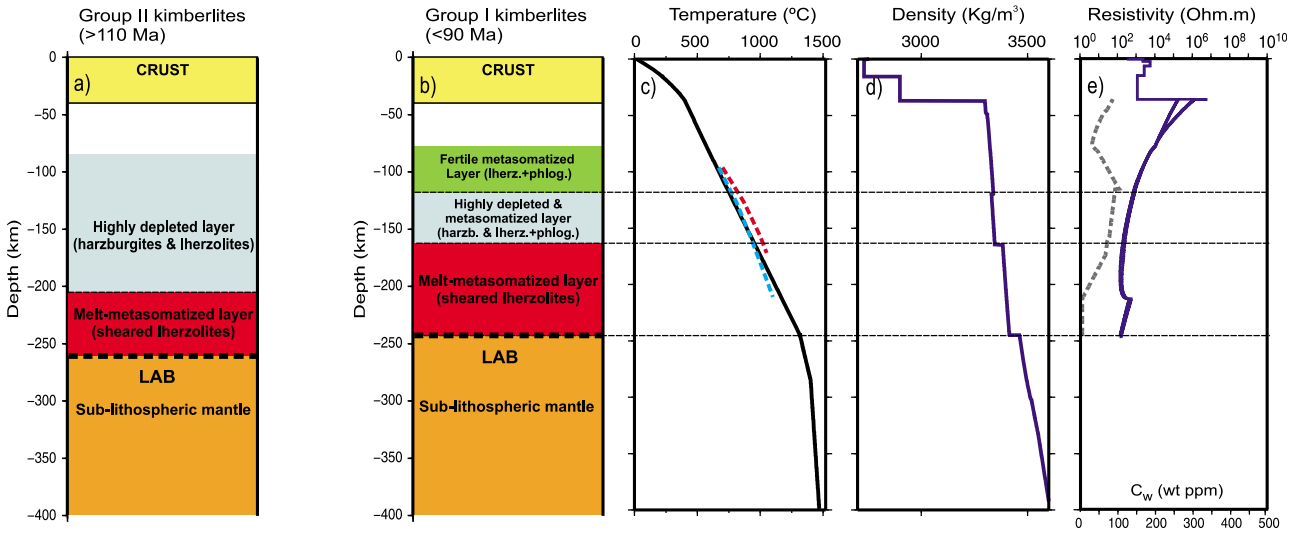

Figure 12. Lithospheric mantle chemical structure in SW Kaapvaal derived from (a) group II kimberlites (>110 Ma) and (b) group I kimberlites (<90 Ma) [after *Griffin et al.*, 2003]. (c) Black line is the calculated geotherm for our preferred model with a thermal LAB depth of 245 km; the red and blue dashed lines are the paleogeotherms for group I and II kimberlites, respectively. Paleogeotherms are determined for peridotitic garnets assuming the Ni thermometer as described by *Griffin et al.* [2003]. (d) Density profile for our preferred model with a thermal LAB of 245 km. (e) Resistivity (blue solid lines, minimum and maximum HS bounds) and water content (gray dashed line) profiles for our preferred model assuming the proton conduction model PC1 (equation (11) and Tables 2 and 3).

group II xenoliths at 120 Ma) after the significant perturbation caused by the Mesozoic thermal or magmatic event that took place between the eruptions of the earlier group II and later group I kimberlites (reflected in the hotter geotherm recorded in group I xenoliths). Such a thermal or magmatic event, whatever its nature, may therefore not have eroded the base of the lithosphere but merely changed its temperature (temporarily) and composition (permanently) because of magmatic (lowermost lithosphere) and metasomatic (depleted and uppermost lithosphere) processes.

6. Conclusions

[65] In this paper we have carefully and systematically reviewed state-of-the-art laboratory studies of the electrical conductivity of the main mantle mineral constituents. Temperature and water content are the most important parameters controlling the electrical conductivity of mantle minerals. Iron content and pressure are of secondary importance.

[66] On the basis of a thorough review of the available experimental results we have defined a bulk conductivity model for the upper mantle which accounts for temperature, pressure and compositional (i.e., water content and X_{Fe}) variations. Different averaging schemes not requiring any assumptions regarding the mineral phase geometry were considered for determining the bulk conductivity of mantle rocks. The bulk electrical conductivity model of the upper mantle has been integrated into the software package LitMod, which allows for petrological and geophysical modeling of the lithosphere and sublithospheric upper mantle within an internally consistent petrological-geophysical framework.

[67] We have modeled the lithospheric structure in the KC and the RT Precambrian terranes using MT, topography, SHF and xenolith data. Our results suggest that for the two terranes the uppermost depleted part of the lithosphere contains more water that the lowermost melt-metasomatized and refertilized lithosphere. The depth of the electrical LAB, as defined by a zone of relatively low resistivity and the cusp in

Figure 11. Sensitivity tests for the MT data for (a–i) the Kaapvaal Craton at site KIM015 and (j–r) the Rehoboth Terrane at site KIM426 (see location in Figure 5) assuming the proton conduction model PC2 (equation (11) and Tables 2 and 3). Bulk resistivity depth profile including the crust (Figures 11a and 11j). In the mantle, the upper and lower Hashin-Shtrikman bounds of the mantle mineral resistivity are shown. The colors correspond to different LAB depth values: red is 200 km (Figure 11a) and 150 km (Figure 11j), black is 230 km (Figure 11a) and 165 km (Figure 11j), and green is 260 km (Figure 11a) and 180 km (Figure 11j). The black dashed line is the bulk water content. Figures 11d, 11g, 11m, and 11p are the same as Figures 11a and 11j but the colors show different water content distributions with depth. The predicted apparent resistivity (Figures 11b, 11e, 11h, 11k, 11n, and 11q) and phase (Figures 11c, 11f, 11i, 11l, 11o, and 11r) for the geometrical average of the Hashin-Shtrikman bounds of the resistivity profiles in Figures 11a, 11d, 11g, 11j, 11m, and 11p are also shown. Black points in Figures 11b, 11c, 11e, 11f, 11h, 11i, 11k, 11l, 11n, 11o, 11q, and 11r represent the observed values with the associated error bars as described in Figure 6. The colors in Figures 11b, 11c, 11e, 11f, 11h, 11i, 11k, 11l, 11n, 11o, 11q, and 11r represent the MT responses for the different resistivity depth profiles in Figures 11a, 11d, 11g, 11j, 11m, and 11p.

the resistivity-depth profile, is controlled by the distribution of water within the lithosphere, and the absolute value of the resistivity profile is determined by both water content and the depth of the thermal LAB. In the case of the KC our estimate of the present-day thermal LAB (230–260 km) suggests a somewhat colder geotherm with respect to that derived from group I kimberlites (circa 90 Ma). We interpret this difference as the result of thermal relaxation after the major Mesozoic thermal/magmatic event that took place between the eruptions of earlier group II and later group I kimberlites that would not have removed the lowermost part of the cratonic root. For the RT our preferred model shows a thermal LAB and wet-dry transition depth of 150 ± 10 and 155 ± 15 km, respectively.

[68] **Acknowledgments.** The SAMTEX data were acquired through funding provided by the Continental Dynamics program of the U.S. National Science Foundation (grant EAR0455242 to R. L. Evans, WHOI), the South African Department of Science and Technology (grant to South African Council for Geoscience), and Science Foundation Ireland (grant 05/RGP/GEO001 to A.G.J.) plus financial and/or logistical support provided by all members of the SAMTEX consortium listed in the acknowledgments of *Jones et al.* [2009b]. Many people strove hard to acquire the SAMTEX data set, and all are very gratefully thanked (see authors and those acknowledged in the work by *Jones et al.* [2009b]). J.F. was supported by an IRCSET grant to A.G.J. for the TopoMed project (TopoMed: Plate reorganization in the western Mediterranean: Lithospheric causes and topographic consequences) within the TOPO-EUROPE EUROCORES.

References

Afonso, J. C., and S. Zlotnik (2011), The subductability of the continental lithosphere: The before and after story, in *Arc-Continent Collision*, edited by D. Brown and P. D. Ryan, pp. 53–86, Springer, New York, doi:10.1007/978-3-540-88558.

Afonso, J. C., M. Fernàndez, G. Ranalli, W. L. Griffin, and J. A. D. Connolly (2008), Integrated geophysical-petrological modeling of the lithosphere and sublithospheric upper mantle: Methodology and applications, *Geochem. Geophys. Geosyst.*, *9*, Q05008, doi:10.1029/2007GC001834.

Allsopp, H. L., J. W. Bristow, C. B. Smith, R. Brown, A. J. W. Gleadow, J. D. Kramers, and O. G. Garvie (1989), A summary of radiometric dating methods applicable to kimberlites and related rocks, in *Kimberlites and Related Rocks*, vol. 1, edited by J. Ross, *Spec. Publ. Geol. Soc. Aust.*, *14*, 343–357.

Artemieva, I. M. (2009), The continental lithosphere: Reconciling thermal, seismic, and petrologic data, *Lithos*, *109*, 23–46, doi:10.1016/j.lithos.2008.09.015.

Baier, B., H. Berckemer, D. Gajewski, R. W. Green, C. Grimsel, C. Prodehl, and R. Vees (1983), Deep seismic sounding in the area of the Damara Orogen, Namibia, south west Africa, in *Intercontinental Fold Belts*, edited by H. Martin and F. W. Eder, pp. 885–900, Springer, New York.

Bailey, R. C. (1970), Inversion of the geomagnetic induction problem, *Proc. R. Soc. London, Ser. A*, *315*, 185–194, doi:10.1098/rspa.1970.0036.

Bali, E., N. Bolfan-Casanova, and K. Koga (2008), Pressure and temperature dependence of H solubility in forsterite: An implication to water activity in the Earth interior, *Earth Planet. Sci. Lett.*, *268*, 354–363, doi:10.1016/j.epsl.2008.01.035.

Bell, D. R., and G. R. Rossman (1992), The distribution of hydroxyl in garnets from the subcontinental mantle of southern Africa, *Contrib. Mineral. Petrol.*, *111*(2), 161–178, doi:10.1007/BF00348949.

Bell, D. R., P. D. Ihinger, and G. R. Rossman (1995), Quantitative analysis of trace OH in garnet and pyroxenes, *Am. Mineral.*, *80*(5–6), 465–474.

Bell, D. R., G. R. Rossman, J. Maldener, D. Endisch, and F. Rauch (2003a), Hydroxide in olivine: A quantitative determination of the absolute amount and calibration of the IR spectrum, *J. Geophys. Res.*, *108*(B2), 2105, doi:10.1029/2001JB000679.

Bell, D. R., M. D. Schmitz, and P. E. Janney (2003b), Mesozoic thermal evolution of the southern African mantle lithosphere, *Lithos*, *71*, 273–287, doi:10.1016/S0024-4937(03)00117-8.

Berryman, J. G. (1995), Mixture theories for rock properties, in *Global Earth Physics: A Handbook of Physical Constants*, edited by T. J. Ahrens, pp. 205–228, AGU, Washington, D. C.

Boyd, F. R., D. G. Pearson, K. O. Hoal, B. G. Hoal, P. H. Nixon, M. J. Kingston, and S. A. Mertzman (2004), Garnet lherzolites from Louwrensia, Namibia: Bulk composition and P/T relations, *Lithos*, *77*(1–4), 573–592, doi:10.1016/j.lithos.2004.03.010.

Carlson, R. W., T. L. Grove, M. J. de Wit, and J. J. Gurney (1996), Anatomy of an Archaean craton: A program for interdisciplinary studies of the Kaapvaal Craton, southern Africa, *Eos Trans. AGU*, *77*, 273–277.

Chevrot, S., and L. Zhao (2007), Multiscale finite-frequency Rayleigh wave tomography of the Kaapvaal Craton, *Geophys. J. Int.*, *169*(1), 201–215, doi:10.1111/j.1365-246X.2006.03289.x.

Christensen, N. I., and W. D. Mooney (1995), Seismic velocity structure and composition of the continental crust: A global view, *J. Geophys. Res.*, *100*(B6), 9761–9788, doi:10.1029/95JB00259.

Connolly, J. A. D. (2005), Computation of phase equilibria by linear programming: A tool for geodynamic modeling and its application to subduction zone decarbonation, *Earth Planet. Sci. Lett.*, *236*(1–2), 524–541, doi:10.1016/j.epsl.2005.04.033.

Constable, S. (2006), SEO3: A new model of olivine electrical conductivity, *Geophys. J. Int.*, *166*(1), 435–437, doi:10.1111/j.1365-246X.2006.03041.x.

Constable, S. C., R. L. Parker, and C. G. Constable (1987), Occam's inversion: A practical algorithm for generating smooth models from electromagnetic sounding data, *Geophysics*, *52*(3), 289–300, doi:10.1190/1.1442303.

Constable, S., T. J. Shankland, and A. Duba (1992), The electrical conductivity of an isotropic olivine mantle, *J. Geophys. Res.*, *97*(B3), 3397–3404, doi:10.1029/91JB02453.

Dai, L., and S.-I. Karato (2009a), Electrical conductivity of pyrope-rich garnet at high temperature and high pressure, *Phys. Earth Planet. Inter.*, *176*(1–2), 83–88, doi:10.1016/j.pepi.2009.04.002.

Dai, L., and S.-I. Karato (2009b), Electrical conductivity of orthopyroxene: Implications for the water content of the asthenosphere, *Proc. Jpn. Acad., Ser. B*, *85*(10), 466–475, doi:10.2183/pjab.85.466.

Dai, L., H. Li, C. Liu, G. Su, and S. Shan (2006), Experimental measurement of the electrical conductivity of pyroxenite at high temperature and high pressure under different oxygen fugacities, *High Pressure Res.*, *26*(3), 193–202, doi:10.1080/08957950600725503.

Davies, G. R., A. J. Spriggs, and P. H. Nixon (2001), A non-cognate origin for the Gibeon kimberlite megacryst suite, Namibia: Implications for the origin of Namibian kimberlites, *J. Petrol.*, *42*, 159–172, doi:10.1093/petrology/42.1.159.

Demouchy, S. (2010), Diffusion of hydrogen in olivine grain boundaries and implications for the survival of water-rich zones in the Earth's mantle, *Earth Planet. Sci. Lett.*, *295*, 305–313, doi:10.1016/j.epsl.2010.04.019.

Demouchy, S., and S. Mackwell (2006), Mechanisms of hydrogen incorporation and diffusion in iron-bearing olivine, *Phys. Chem. Miner.*, *33*(5), 347–355, doi:10.1007/s00269-006-0081-2.

Demouchy, S., S. D. Jacobsen, F. Gaillard, and C. R. Stern (2006), Rapid magma ascent recorded by water diffusion profiles in mantle olivine, *Geology*, *34*(6), 429–432, doi:10.1130/G22386.1.

de Wit, M. J., C. Roering, R. J. Hart, R. A. Armstrong, C. E. J. de Ronde, R. W. E. Green, M. Tredoux, E. Peberdy, and R. A. Hart (1992), Formation of Archaean continent, *Nature*, *357*, 553–562, doi:10.1038/357553a0.

Du Frane, W. L., J. J. Roberts, D. A. Toffelmier, and J. A. Tyburczy (2005), Anisotropy of electrical conductivity in dry olivine, *Geophys. Res. Lett.*, *32*, L24315, doi:10.1029/2005GL023879.

Duba, A. (1976), Are laboratory electrical conductivity data relevant to the Earth?, *Acta Geodaet. Geophys. Montanist. Acad. Sci. Hung.*, *11*, 485–496.

Durrheim, R. J. (1998), Seismic refraction investigations of the Kaapvaal Craton, *S. Afr. Geophys. Rev.*, *2*, 29–35.

Durrheim, R. J., and W. D. Mooney (1991), Archean and Proterozoic crustal evolution: Evidence from crustal seismology, *Geology*, *19*(6), 606–609, doi:10.1130/0091-7613(1991)019<0606:AAPCEE>2.3.CO;2.

Eaton, D. W., F. Darbyshire, R. L. Evans, H. Grütter, A. G. Jones, and X. Yuan (2009), The elusive lithosphere-asthenosphere boundary (LAB) beneath cratons, *Lithos*, *109*(1–2), 1–22, doi:10.1016/j.lithos.2008.05.009.

Evans, R. L., et al. (2011), Electrical lithosphere beneath the Kaapvaal Craton, southern Africa, *J. Geophys. Res.*, *116*, B04105, doi:10.1029/2010JB007883.

Farla, R., C. Peach, and S. ten Grotenhuis (2010), Electrical conductivity of synthetic iron-bearing olivine, *Phys. Chem. Miner.*, *37*(3), 167–178, doi:10.1007/s00269-009-0321-3.

Ferot, A., and N. Bolfan-Casanova (2010), Experimentally determined water storage capacity in the Earth's upper mantle, Abstract 1440H–V23E presented at 2010 Fall Meeting, AGU, San Francisco, Calif.

Fouch, M. J., D. E. James, J. C. VanDecar, S. van der Lee, and the Kaapvaal Seismic Group (2004), Mantle seismic structure beneath the Kaapvaal

and Zimbabwe cratons, *S. Afr. J. Geol.*, *107*(1–2), 33–44, doi:10.2113/107.1-2.33.

Freybourger, M., J. B. Gaherty, T. H. Jordan, and Kaapvaal Seismic Group (2001), Structure of the Kaapvaal Craton from surface waves, *Geophys. Res. Lett.*, *28*(13), 2489–2492, doi:10.1029/2000GL012436.

Fullea, J., J. C. Afonso, J. A. D. Connolly, M. Fernàndez, D. García-Castellanos, and H. Zeyen (2009), LitMod3D: An interactive 3-D software to model the thermal, compositional, density, seismological, and rheological structure of the lithosphere and sublithospheric upper mantle, *Geochem. Geophys. Geosyst.*, *10*, Q08019, doi:10.1029/2009GC002391.

Gaillard, F., M. Malki, G. Iacono-Marziano, M. Pichavant, and B. Scaillet (2008), Carbonatite melts and electrical conductivity in the asthenosphere, *Science*, *322*(5906), 1363–1365, doi:10.1126/science.1164446.

Gatzemeier, A., and M. Moorkamp (2005), 3D modelling of electrical anisotropy from electromagnetic array data: Hypothesis testing for different upper mantle conduction mechanisms, *Phys. Earth Planet. Inter.*, *149*(3–4), 225–242, doi:10.1016/j.pepi.2004.10.004.

Gatzemeier, A., and A. Tommasi (2006), Flow and electrical anisotropy in the upper mantle: Finite-element models constraints on the effects of olivine crystal preferred orientation and microstructure, *Phys. Earth Planet. Inter.*, *158*(2–4), 92–106, doi:10.1016/j.pepi.2006.01.009.

Gavrilenko, P. (2008), Water solubility in diopside, Ph.D. thesis, Bayerisches Geoinst., Univ. Bayreuth, Bayreuth, Germany.

Gose, J., P. Reichart, G. Dollinger, and E. Schmädicke (2008), Water in natural olivine—Determined by proton-proton scattering analysis, *Am. Mineral.*, *93*, 1613–1619, doi:10.2138/am.2008.2835.

Grant, K., J. Ingrin, J. Lorand, and P. Dumas (2007), Water partitioning between mantle minerals from peridotite xenoliths, *Contrib. Mineral. Petrol.*, *154*(1), 15–34, doi:10.1007/s00410-006-0177-1.

Griffin, W. L., S. Y. O'Reilly, N. Abe, S. Aulbach, R. M. Davies, N. J. Pearson, B. J. Doyle, and K. Kivi (2003), The origin and evolution of Archean lithospheric mantle, *Precambrian Res.*, *127*(1–3), 19–41, doi:10.1016/S0301-9268(03)00180-3.

Groom, R. W., and R. C. Bailey (1989), Decomposition of magnetotelluric impedance tensors in the presence of local three-dimensional galvanic distortion, *J. Geophys. Res.*, *94*(B2), 1913–1925, doi:10.1029/JB094iB02p01913.

Grütter, H. S., D. B. Apter, and J. Kong (1999), Crust-mantle coupling: Evidence from mantle-derived xenocrystic garnets, in *Proceedings of the 7th International Kimberlite Conference*, edited by J. J. Gurney et al., pp. 307–313, Red Roof Design, Cape Town, South Africa.

Grütter, H., D. Latti, and A. Menzies (2006), Cr-saturation arrays in concentrate garnet compositions from kimberlite and their use in mantle barometry, *J. Petrol.*, *47*(4), 801–820, doi:10.1093/petrology/egi096.

Gurnis, M., J. X. Mitrovica, J. Ritsema, and H.-J. van Heijst (2000), Constraining mantle density structure using geological evidence of surface uplift rates: The case of the African Superplume, *Geochem. Geophys. Geosyst.*, *1*(7), 1020, doi:10.1029/1999GC000035.

Hammouda, T., and D. Laporte (2000), Ultrafast mantle impregnation by carbonatite melts, *Geology*, *28*(3), 283–285, doi:10.1130/0091-7613(2000)28<283:UMIBCM>2.0.CO;2.

Hansen, S. E., A. A. Nyblade, J. Julià, P. H. G. M. Dirks, and R. J. Durrheim (2009), Upper-mantle low-velocity zone structure beneath the Kaapvaal Craton from *S*-wave receiver functions, *Geophys. J. Int.*, *178*(2), 1021–1027, doi:10.1111/j.1365-246X.2009.04178.x.

Hashin, Z., and S. Shtrikman (1963), A variational approach to the theory of the elastic behaviour of multiphase materials, *J. Mech. Phys. Solids*, *11*, 127–140, doi:10.1016/0022-5096(63)90060-7.

Hinze, E. (1982), Laboratory electrical conductivity measurements on mantle relevant minerals, *Geophys. Surv.*, *4*, 337–352, doi:10.1007/BF01449105.

Hinze, H., G. Will, and L. Cemic (1981), Electrical conductivity measurements on synthetic olivines and on olivine, enstatite and diopside from Dreiser Weiher, Eifel (Germany) under defined thermodynamic activities as a function of temperature and pressure, *Phys. Earth Planet. Inter.*, *25*(3), 245–254, doi:10.1016/0031-9201(81)90068-6.

Hirsch, L. M., T. J. Shankland, and A. G. Duba (1993), Electrical conduction and polaron mobility in Fe-bearing olivine, *Geophys. J. Int.*, *114*(1), 36–44, doi:10.1111/j.1365-246X.1993.tb01464.x.

Hirschmann, M. M. (2006), Water, melting, and the deep Earth H_2O cycle, *Annu. Rev. Earth Planet. Sci.*, *34*(1), 629–653, doi:10.1146/annurev.earth.34.031405.125211.

Hirth, G., R. L. Evans, and A. D. Chave (2000), Comparison of continental and oceanic mantle electrical conductivity: Is the Archean lithosphere dry?, *Geochem. Geophys. Geosyst.*, *1*, 1030, doi:10.1029/2000GC000048.

Hoal, B. G., K. E. O. Hoal, F. R. Boyd, and D. G. Pearson (1995), Age constraints on crustal and mantle lithosphere beneath the Gibeon kimberlite field, Namibia, *S. Afr. J. Geol.*, *98*, 112–118.

Holland, T. J. B., and R. Powell (1998), An internally consistent thermodynamic dataset for phases of petrological interest, *J. Metamorph. Geol.*, *16*, 309–343, doi:10.1111/j.1525-1314.1998.00140.x.

Holtzman, B. K., N. J. Groebner, M. E. Zimmerman, S. B. Ginsberg, and D. Kohlstedt (2003), Stress-driven melt segregation in partially molten rocks, *Geochem. Geophys. Geosyst.*, *4*(5), 8607, doi:10.1029/2001GC000258.

Irifune, T., and A. E. Ringwood (1987), Phase transformations in a harzburgite composition to 26 GPa: Implications for dynamical behaviour of the subducting slab, *Earth Planet. Sci. Lett.*, *86*(2–4), 365–376, doi:10.1016/0012-821X(87)90233-0.

Jacobs, J., S. Pisarevsky, R. J. Thomas, and T. Becker (2008), The Kalahari Craton during the assembly and dispersal of Rodinia, *Precambrian Res.*, *160*, 142–158, doi:10.1016/j.precamres.2007.04.022.

Jaupart, C. (1983), Horizontal heat transfer due to radioactivity contrasts: Causes and consequences of the linear heat flow relation, *Geophys. J. R. Astron. Soc.*, *75*(2), 411–435.

Jaupart, C., and J.-C. Mareschal (2003), Constraints on crustal heat production from heat flow data, in *Treatise of Geochemistry: The Crust*, edited by R. L. Rudnick, pp. 65–84, Elsevier, Amsterdam, doi:10.1016/B0-08-043751-6/03017-6.

Jelsma, H. A., M. de Wit, C. Thiart, P. H. G. M. Dirks, G. Viola, I. J. Basson, and E. Anckar (2004), Preferential distribution along transcontinental corridors of kimberlites and related rocks of southern Africa, *S. Afr. J. Geol.*, *107*, 301–324, doi:10.2113/107.1-2.301.

Jones, M. Q. W. (1998), A review of heat flow in southern Africa and the thermal structure of the lithosphere, *S. Afr. Geophys. Rev.*, *2*, 115–122.

Jones, A. G. (1999), Imaging the continental upper mantle using electromagnetic methods, *Lithos*, *48*(1–4), 57–80.

Jones, A. G., R. L. Evans, and D. W. Eaton (2009a), Velocity-conductivity relationships for mantle mineral assemblages in Archean cratonic lithosphere based on a review of laboratory data and Hashin-Shtrikman extremal bounds, *Lithos*, *109*(1–2), 131–143, doi:10.1016/j.lithos.2008.10.014.

Jones, A. G., et al. (2009b), Area selection for diamonds using magnetotellurics: Examples from southern Africa, *Lithos*, *112*, suppl. 1, 83–92, doi:10.1016/j.lithos.2009.06.011.

Karato, S. (1990), The role of hydrogen in the electrical conductivity of the upper mantle, *Nature*, *347*(6290), 272–273, doi:10.1038/347272a0.

Karato, S.-I., and L. Dai (2009), Comments on "Electrical conductivity of wadsleyite as a function of temperature and water content" by Manthilake et al., *Phys. Earth Planet. Inter.*, *174*(1–4), 19–21, doi:10.1016/j.pepi.2009.01.011.

Kelbert, A., A. Schultz, and G. Egbert (2009), Global electromagnetic induction constraints on transition-zone water content variations, *Nature*, *460*(7258), 1003–1006, doi:10.1038/nature08257.

Kgaswane, E. M., A. A. Nyblade, J. Julià, P. H. G. M. Dirks, R. J. Durrheim, and M. E. Pasyanos (2009), Shear wave velocity structure of the lower crust in southern Africa: Evidence for compositional heterogeneity within Archaean and Proterozoic terrains, *J. Geophys. Res.*, *114*, B12304, doi:10.1029/2008JB006217.

Kobussen, A. F., W. L. Griffin, S. Y. O'Reilly, and S. R. Shee (2008), Ghosts of lithospheres past: Imaging an evolving lithospheric mantle in southern Africa, *Geology*, *36*(7), 515–518, doi:10.1130/G24868A.1.

Kohlstedt, D. L., and S. J. Mackwell (1998), Diffusion of hydrogene and intrinsic point defects in olivine, *Z. Phys. Chem.*, *207*, 147–162.

Kozlovskaya, E., and S. E. Hjelt (2000), Modeling of elastic and electrical properties of solid-liquid rock system with fractal microstructure, *Phys. Chem. Earth, Part A*, *25*(2), 195–200, doi:10.1016/S1464-1895(00)00031-4.

Laštovičková, M. (1983), Laboratory measurements of electrical properties of rocks and minerals, *Geophys. Surv.*, *6*, 201–213, doi:10.1007/BF01454001.

Laštovičková, M. (1991), A review of laboratory measurements of the electrical conductivity of rocks and minerals, *Phys. Earth Planet. Inter.*, *66*(1–2), 1–11, doi:10.1016/0031-9201(91)90099-4.

Ledo, J., and A. G. Jones (2005), Upper mantle temperature determined from combining mineral composition, electrical conductivity laboratory studies and magnetotelluric field observations: Application to the intermontane belt, Northern Canadian Cordillera, *Earth Planet. Sci. Lett.*, *236*(1–2), 258–268, doi:10.1016/j.epsl.2005.01.044.

Li, A. (2011), Shear wave model of southern Africa from regional Rayleigh wave tomography with 2-D sensitivity kernels, *Geophys. J. Int.*, *185*(2), 832–844, doi:10.1111/j.1365-246X.2011.04971.x.

Li, A., and K. Burke (2006), Upper mantle structure of southern Africa from Rayleigh wave tomography, *J. Geophys. Res.*, *111*, B10303, doi:10.1029/2006JB004321.

Li, Z.-X. A., C.-T. A. Lee, A. H. Peslier, A. Lenardic, and S. J. Mackwell (2008), Water contents in mantle xenoliths from the Colorado Plateau and vicinity: Implications for the mantle rheology and hydration-induced

thinning of continental lithosphere, *J. Geophys. Res.*, *113*, B09210, doi:10.1029/2007JB005540.
Lizarralde, D., A. Chave, G. Hirth, and A. Schultz (1995), Northeastern Pacific mantle conductivity profile from long-period magnetotelluric sounding using Hawaii-to-California submarine cable data, *J. Geophys. Res.*, *100*(B9), 17,837–17,854, doi:10.1029/95JB01244.
Lu, R., and H. Keppler (1997), Water solubility in pyrope to 100 kbar, *Contrib. Mineral. Petrol.*, *129*(1), 35–42, doi:10.1007/s004100050321.
Maxwell-Garnett, J. C. M. (1904), Colours in metal glasses and in metallic films, *Philos. Trans. R. Soc. London, Ser. A*, *203*(359–371), 385–420.
McDonough, W. F., and S.-S. Sun (1995), The composition of the Earth, *Chem. Geol.*, *120*, 223–253.
Mierdel, K., H. Keppler, J. R. Smyth, and F. Langenhorst (2007), Water solubility in aluminous orthopyroxene and the origin of Earth's asthenosphere, *Science*, *315*(5810), 364–368, doi:10.1126/science.1135422.
Mookherjee, M., and S.-I. Karato (2010), Solubility of water in pyrope-rich garnet at high pressures and temperature, *Geophys. Res. Lett.*, *37*, L03310, doi:10.1029/2009GL041289.
Moorkamp, M., A. G. Jones, and S. Fishwick (2010), Joint inversion of receiver functions, surface wave dispersion and magnetotelluric data, *J. Geophys. Res.*, *115*, B04318, doi:10.1029/2009JB006369.
Muller, M. R., et al. (2009), Lithospheric structure, evolution and diamond prospectivity of the Rehoboth Terrane and western Kaapvaal Craton, southern Africa: Constraints from broadband magnetotellurics, *Lithos*, *112*, suppl. 1, 93–105, doi:10.1016/j.lithos.2009.06.023.
Nair, S. K., S. S. Gao, K. H. Liu, and P. G. Silver (2006), Southern African crustal evolution and composition: Constraints from receiver function studies, *J. Geophys. Res.*, *111*, B02304, doi:10.1029/2005JB003802.
Nguuri, T. K., J. Gore, D. E. James, S. J. Webb, C. Wright, T. G. Zengeni, O. Gwavava, J. A. Snoke, and Kaapvaal Seismic Group (2001), Crustal structure beneath southern Africa and its implications for the formation and evolution of the Kaapvaal and Zimbabwe cratons, *Geophys. Res. Lett.*, *28*(13), 2501–2504, doi:10.1029/2000GL012587.
Nicolaysen, L. O., R. J. Hart, and N. H. Gale (1981), The Vredefort radioelement profile extended to supracrustal strata at Carletonville, with implications for continental heat flow, *J. Geophys. Res.*, *86*(B11), 10,653–10,661, doi:10.1029/JB086iB11p10653.
Nover, G. (2005), Electrical properties of crustal and mantle rocks—A review of laboratory measurements and their explanation, *Surv. Geophys.*, *26*, 593–651, doi:10.1007/s10712-005-1759-6.
Nyblade, A. A., and H. N. Pollack (1993), A global analysis of heat flow from Precambrian terrains: Implications for the thermal structure of Archean and Proterozoic lithosphere, *J. Geophys. Res.*, *98*(B7), 12,207–12,218, doi:10.1029/93JB00521.
Nyblade, A. A., and S. W. Robinson (1994), The African Superswell, *Geophys. Res. Lett.*, *21*(9), 765–768, doi:10.1029/94GL00631.
Nyblade, A. A., and N. H. Sleep (2003), Long lasting epeirogenic uplift from mantle plumes and the origin of the Southern African Plateau, *Geochem. Geophys. Geosyst.*, *4*(12), 1105, doi:10.1029/2003GC000573.
O'Reilly, S. Y., and W. L. Griffin (2010), The continental lithosphere-asthenosphere boundary: Can we sample it?, *Lithos*, *120*(1–2), 1–13, doi:10.1016/j.lithos.2010.03.016.
Omura, K., K. Kurita, and M. Kumazawa (1989), Experimental study of pressure dependence of electrical conductivity of olivine at high temperatures, *Phys. Earth Planet. Inter.*, *57*(3–4), 291–303, doi:10.1016/0031-9201(89)90118-0.
Paterson, M. (1982), The determination of hydroxyl by infrared absorption in quartz, silicate glasses and minerals, *Bull. Mineral*, *105*, 20–29.
Peslier, A. H. (2010), A review of water contents of nominally anhydrous natural minerals in the mantles of Earth, Mars and the Moon, *J. Volcanol. Geotherm. Res.*, *197*(1–4), 239–258, doi:10.1016/j.jvolgeores.2009.10.006.
Peslier, A. H., and J. F. Luhr (2006), Hydrogen loss from olivines in mantle xenoliths from Simcoe (USA) and Mexico: Mafic alkalic magma ascent rates and water budget of the sub-continental lithosphere, *Earth Planet. Sci. Lett.*, *242*(3–4), 302–319, doi:10.1016/j.epsl.2005.12.019.
Peslier, A. H., A. B. Woodland, D. R. Bell, and M. Lazarov (2010), Olivine water contents in the continental lithosphere and the longevity of cratons, *Nature*, *467*, 78–81, doi:10.1038/nature09317.
Pitzer, K. S., and S. M. Sterner (1995), Equations of state valid continuously from zero to extreme pressures with H_2O and CO_2 as examples, *Int. J. Thermophys.*, *16*(2), 511–518, doi:10.1007/BF01441917.
Poe, B. T., C. Romano, F. Nestola, and J. R. Smyth (2010), Electrical conductivity anisotropy of dry and hydrous olivine at 8 GPa, *Phys. Earth Planet. Inter.*, *181*(3–4), 103–111, doi:10.1016/j.pepi.2010.05.003.
Pollack, H. N., and D. S. Chapman (1977), Mantle heat flow, *Earth Planet. Sci. Lett.*, *34*(2), 174–184, doi:10.1016/0012-821X(77)90002-4.
Pommier, A., F. Gaillard, M. Pichavant, and B. Scaillet (2008), Laboratory measurements of electrical conductivities of hydrous and dry Mount Vesuvius melts under pressure, *J. Geophys. Res.*, *113*, B05205, doi:10.1029/2007JB005269.
Priestley, K., D. McKenzie, and E. Debayle (2006), The state of the upper mantle beneath southern Africa, *Tectonophysics*, *416*, 101–112.
Ringwood, A. E. (1975), *Composition and Petrology of the Earth's Mantle*, McGraw-Hill, New York.
Romano, C., B. T. Poe, N. Kreidie, and C. A. McCammon (2006), Electrical conductivities of pyrope-almandine garnets up to 19 GPa and 1700°C, *Am. Mineral.*, *91*, 1371–1377, doi:10.2138/am.2006.1983.
Rudnick, R. L., W. F. McDonough, and R. J. O'Connell (1998), Thermal structure, thickness and composition of continental lithosphere, *Chem. Geol.*, *145*(3–4), 395–411, doi:10.1016/S0009-2541(97)00151-4.
Schmitz, M. D., S. A. Bowring, M. J. de Wit, and V. Gartz (2004), Subduction and terrane collision stabilise the western Kaapvaal Craton tectosphere 2.9 billion years ago, *Earth Planet. Sci. Lett.*, *222*, 363–376, doi:10.1016/j.epsl.2004.03.036.
Schock, R. N., A. Duba, and T. J. Shankland (1989), Electric conduction in olivine, *J. Geophys. Res.*, *94*(B5), 5829–5839, doi:10.1029/JB094iB05p05829.
Schulgasser, K. (1976), Relationship between single-crystal and polycrystal electrical conductivity, *J. Appl. Phys.*, *47*(5), 1880–1886, doi:10.1063/1.322907.
Schulgasser, K. (1977), Bounds on the conductivity of statistically isotropic polycrystals, *J. Phys. C Solid State Phys.*, *10*, 407–417, doi:10.1088/0022-3719/10/3/011.
Seifert, K. F., G. Will, and R. Voigt (1982), Electrical conductivity measurements on synthetic pyroxenes $MgSiO_3$-$FeSiO_3$ at high pressures and temperatures under defined thermodynamic conditions, in *High-Pressure Researches in Geoscience*, edited by W. Schreyer, pp. 419–432, Schweizerbartsche, Stuttgart, Germany.
Spangenberg, E. (1998), A fractal model for physical properties of porous rock: Theoretical formulations and application to elastic properties, *J. Geophys. Res.*, *103*(B6), 12,269–12,289, doi:10.1029/98JB00600.
Spriggs, A. J. (1988), An isotopic and geochemical study of kimberlites and associated alkaline rocks from Namibia, Ph.D. thesis, Univ. of Leeds, Leeds, U. K.
Toffelmier, D. A., and J. A. Tyburczy (2007), Electromagnetic detection of a 410-km-deep melt layer in the southwestern United States, *Nature*, *447*(7147), 991–994, doi:10.1038/nature05922.
Tyburczy, J. A., and H. S. Waff (1983), Electrical conductivity of molten basalt and andesite to 25 kilobars pressure: Geophysical significance and implications for charge transport and melt structure, *J. Geophys. Res.*, *88*(B3), 2413–2430, doi:10.1029/JB088iB03p02413.
Vacher, P., and O. Verhoeven (2007), Modelling the electrical conductivity of iron-rich minerals for planetary applications, *Planet. Space Sci.*, *55*(4), 455–466, doi:10.1016/j.pss.2006.10.003.
Wait, J. R. (1954), On the relation between telluric currents and the Earth's magnetic field, *Geophysics*, *19*(2), 281–289, doi:10.1190/1.1437994.
Wang, D., M. Mookherjee, Y. Xu, and S.-I. Karato (2006), The effect of water on the electrical conductivity of olivine, *Nature*, *443*(7114), 977–980, doi:10.1038/nature05256.
Wang, Z., S. Ji, and G. Dresen (1999), Hydrogen-enhanced electrical conductivity of diopside crystals, *Geophys. Res. Lett.*, *26*(6), 799–802, doi:10.1029/1999GL900094.
Withers, A. C., B. J. Wood, and M. R. Carroll (1998), The OH content of pyrope at high pressure, *Chem. Geol.*, *147*(1–2), 161–171, doi:10.1016/S0009-2541(97)00179-4.
Xia, Q.-K., Y.-M. Sheng, X.-Z. Yang, and H.-M. Yu (2005), Heterogeneity of water in garnets from UHP eclogites, eastern Dabieshan, China, *Chem. Geol.*, *224*(4), 237–246, doi:10.1016/j.chemgeo.2005.08.003.
Xu, Y., and T. J. Shankland (1999), Electrical conductivity of orthopyroxene and its high pressure phases, *Geophys. Res. Lett.*, *26*(17), 2645–2648, doi:10.1029/1999GL008378.
Xu, Y., T. J. Shankland, and B. T. Poe (2000), Laboratory-based electrical conductivity in the Earth's mantle, *J. Geophys. Res.*, *105*(B12), 27,865–27,875, doi:10.1029/2000JB900299.
Yoshino, T. (2010), Laboratory electrical conductivity measurement of mantle minerals, *Surv. Geophys.*, *31*(2), 163–206, doi:10.1007/s10712-009-9084-0.
Yoshino, T., G. Manthilake, T. Matsuzaki, and T. Katsura (2008a), Dry mantle transition zone inferred from the conductivity of wadsleyite and ringwoodite, *Nature*, *451*(7176), 326–329, doi:10.1038/nature06427.
Yoshino, T., M. Nishi, T. Matsuzaki, D. Yamazaki, and T. Katsura (2008b), Electrical conductivity of majorite garnet and its implications for electrical structure in the mantle transition zone, *Phys. Earth Planet. Inter.*, *170*(3–4), 193–200, doi:10.1016/j.pepi.2008.04.009.
Yoshino, T., T. Matsuzaki, A. Shatskiy, and T. Katsura (2009), The effect of water on the electrical conductivity of olivine aggregates and its impli-

cations for the electrical structure of the upper mantle, *Earth Planet. Sci. Lett.*, *288*(1–2), 291–300, doi:10.1016/j.epsl.2009.09.032.

Zhao, M., C. A. Langston, A. A. Nyblade, and T. J. Owens (1999), Upper mantle velocity structure beneath southern Africa from modeling regional seismic data, *J. Geophys. Res.*, *104*(B3), 4783–4794, doi:10.1029/1998JB900058.

Zhao, Y.-H., S. B. Ginsberg, and D. L. Kohlstedt (2004), Solubility of hydrogen in olivine: Dependence on temperature and iron content, *Contrib. Mineral. Petrol.*, *147*(2), 155–161, doi:10.1007/s00410-003-0524-4.

Ziegler, U. R. F., and G. F. U. Stoessel (1991), Note: New constraints on the age of the Weener Intrusive Suite, the Gamsberg Granite and the crustal evolution of the Rehoboth Basement Inlier, Namibia, *Commun. Geol. Surv. Namibia*, *7*, 75–78.

J. Fullea, A. G. Jones, and M. R. Muller, Dublin Institute for Advanced Studies, 5 Merrion Sq., Dublin 2, Ireland. (jfullea@cp.dias.ie)